

**TSUNAMI BENCHMARK RESULTS FOR THE
NON-HYDROSTATIC WAVE MODEL
NHWAVE, VERSION 3.0**

BY

CHENG ZHANG¹, BABAK TEHRANIRAD¹, JAMES T. KIRBY¹,
MORTEZA DERAKHTI¹, FATEMEH NEMATI², STEPHAN GRILLI²,
GANGFENG MA³, AND FENGYAN SHI¹

¹ CENTER FOR APPLIED COASTAL RESEARCH, DEPARTMENT OF CIVIL AND
ENVIRONMENTAL ENGINEERING, UNIVERSITY OF DELAWARE, NEWARK, DE 19716

² DEPARTMENT OF OCEAN ENGINEERING, UNIVERSITY OF RHODE ISLAND,
NARRAGANSETT, RI 02882

³ DEPARTMENT OF CIVIL AND ENVIRONMENTAL ENGINEERING, OLD DOMINION
UNIVERSITY, NORFOLK, VA 23529

RESEARCH REPORT NO. CACR-17-03

WORK PREPARED IN SUPPORT OF ACTIVITIES FUNDED BY THE
NATIONAL TSUNAMI HAZARD MITIGATION PROGRAM (NOAA)

MAY 2, 2017



CENTER FOR APPLIED COASTAL RESEARCH

University of Delaware
Newark, Delaware 19716

Abstract

This report describes tsunami benchmark testing of version 3.0 of the non-hydrostatic wave model NHWAVE, carried out in support of activities funded by the National Tsunami Hazard Mitigation Program (NTHMP). This report briefly describes the model and details its application to the required benchmarks specified for the 2011 Tsunami Inundation Model Validation Workshop (NTHMP, 2012) and the 2015 current modeling workshop (NTHMP, 2015).

NHWAVE is copyrighted under the terms of the Gnu Public License (GPL); refer to <https://www.gnu.org/licenses/gpl-3.0.en.html>. Present and updated versions of the code may be obtained online from Github, at @JimKirby/NHWAVE. The code distribution includes the required data and input files for generating the model results described in this report.

Contents

1	Introduction	1
2	Model description	2
2.1	Navier-Stokes equations	2
2.2	Governing equations in σ coordinate system	2
2.3	Turbulence Model	5
2.3.1	Standard $k - \epsilon$	6
2.3.2	Renormalization Group (RNG) $k - \epsilon$	6
3	Numerical method	7
3.1	Grid configuration	7
3.2	Time Stepping	7
3.3	Spatial finite volume scheme	9
3.4	Boundary conditions	11
3.5	Basic hydrodynamic considerations	12
3.5.1	Mass conservation	13
3.5.2	Convergence	13
4	Inundation benchmarks	15
4.1	Solitary wave on a simple beach: analytical	15
4.2	Solitary wave on a planar laboratory beach	20
4.3	Solitary wave on a conical island	22
4.4	Tsunami run-up onto a complex 3-D beach; Monai Valley	27
5	Current benchmarks	31
5.1	Flow over a submerged conical mound	31
5.2	Tsunami currents in Hilo Harbor	34
6	Conclusions	39

List of Figures

1	Layout of computational variables. Velocities (u, v, w) are placed at cell center and dynamic pressure p is defined at vertical cell face.	8
2	Convergence rate of the case.	14
3	Definition sketch for simple beach bathymetry(from Synolakis et al (2007, Figure A1)).	15
4	Numerical simulation data for maximum runup of nonbreaking waves climbing up different beach slopes. Solid line represents the runup law (25).	17
5	Water level profiles during runup of the non-breaking wave in the case of $H/d = 0.019$ on a 1:19.85 beach. Dotted red lines represent the analytical solution in according to Synolakis(1986), dashed black lines represent the numerical simulation, and solid blue lines represent the beach.	18
6	The water level dynamics at two locations $X/d = 0.25$ (top) and $X/d = 9.95$ (bottom). Dotted red lines represent the analytical solution in according to Synolakis(1986), and dashed black lines represent the numerical simulation.	19
7	Time evolution of nonbreaking $H/d = 0.0185$ initial wave. Dotted red lines represent the experimental data, dashed black lines represent the numerical simulation, and solid blue lines represent the beach.	20
8	Time evolution of breaking $H/d = 0.3$ initial wave. Dotted red lines represent the experimental data, dashed black lines represent the numerical simulation, and solid blue lines represent the beach.	21
9	View of conical island(top) and basin(bottom)(from Synolakis et al (2007, Figure A16)).	23
10	Definition sketch for conical island. All dimensions are in cm (from Synolakis et al (2007, Figure A17)).	23
11	Schematic gauge locations around the conical island(from Synolakis et al (2007, Figure A18)).	24
12	Comparison of computed and measured time series of free surface for $H/d = 0.045$. Dotted red lines represent the experimental data, and dashed black lines represent the numerical simulation.	25
13	Comparison of computed and measured time series of free surface for $H/d = 0.091$. Dotted red lines represent the experimental data, and dashed black lines represent the numerical simulation.	25
14	Comparison of computed and measured time series of free surface for $H/d = 0.181$. Dotted red lines represent the experimental data, and dashed black lines represent the numerical simulation.	26
15	Comparison of computed and measured maximum runup heights for $H/d = 0.045$ (top), $H/d = 0.091$ (middle) and $H/d = 0.181$ (bottom). Dotted red lines represent the experimental data, and dashed black lines represent the numerical simulation.	26

16	Bathymetry profile of Monai Valley experiment setup (from Synolakis et al (2007, Figure A24)).	27
17	Initial wave profile for Monai Valley experiment and simulation.	28
18	Comparison between extracted movie frames from the overhead movie of the laboratory experiment (left) (from http://burn.giseis.alaska.edu/file doed/Dmitry/BM7 description.zip) and numerical simulation (right).	29
19	Time history of surface elevations at gauges 5, 7 and 9. Solid blue lines represent the experimental data, and dashed black lines represent the numerical simulation.	30
20	Definition sketch for case SB4_02 of flow over a submerged conical mound.	31
21	Comparison of velocity components between numerical results and experimental data at measurement locations. Black circles and lines represent the experimental data, and solid blue lines represent the numerical simulation.	32
22	Comparison of velocity components for three different bottom roughness heights. Solid blue lines represent the results of $k_s = 0.0015\text{mm}$, solid red lines represent the results of $k_s = 0.015\text{mm}$, and dashed black lines represent the results of $k_s = 0.0\text{mm}$	33
23	A snapshot of the vortex train behind the mound for $k_s = 0.0015\text{mm}$	33
24	Bathymetry data from Hilo Harbor with the simulation control point (white dot), the tidal station (grey dot) and the two ADCP locations (black dots)(from http://coastal.usc.edu/currents_workshop/problems/prob2.html).	34
25	Time history of surface elevation at CP. Blue circles and lines represent the field data, solid red lines represent the numerical results from FUNWAVE, and solid black lines represent the numerical results from NHWAVE.	35
26	Time histories of surface elevation at TG (top) and of velocity magnitude at ADCP1 (middle) and ADCP2 (bottom). Blue circles and lines represent the field data, solid red lines represent the numerical results from FUNWAVE, and solid black lines represent the numerical results from NHWAVE.	36
27	Comparison of results from grid G4, G5 and G6 at CP (first layer), TG (second layer), ADCP1 (third layer) and ADCP2 (last layer). Dashed blue lines represent the results with grid G4, solid black lines represent the results with grid G5, and dashed red lines represent the results with grid G6.	37
28	Snapshots of vertical vorticity at two moments showing ADCP1 (left dot) and ADCP2 (middle dot) with G5.	38
29	Maximum predicted fluid speed during entire duration of the 10-m resolution (G5) simulation.	38

List of Tables

1	Maximum runup for analytical case of solitary wave on a simple beach with different grid size.	14
2	Runup data from numerical calculations compared with runup law values.	16
3	NRMSD and maximum wave amplitude errors of numerical results compared to analytical solutions.	17
4	NRMSD and maximum wave amplitude errors of numerical results compared to experimental data.	21
5	NRMSD and maximum wave amplitude errors of numerical results compared to experimental data.	22
6	NRMSD of numerical results compared to experimental data.	22
7	NRMSD of numerical results compared to experimental data.	28

1 Introduction

This report describes testing of the performance of the model NHWAVE, using benchmarks specified by NTHMP for modeling inundation and model-generated current fields.

NHWAVE is a fully nonlinear, non-hydrostatic, 3D solver for surface wave motion developed by Ma et al (2012) and Derakhti et al (2016a). NHWAVE solves either the Euler equations or Reynolds-averaged Navier-Stokes (RANS) equations in a time-dependent, surface- and bottom-following σ coordinate system. The code may also be configured to perform Large-eddy Simulations (LES), but this option was not employed in the present study. In RANS applications, turbulent stresses are represented through use of a $k - \epsilon$ closure.

NHWAVE is presently used in NTHMP-funded work to perform simulations of the initial source region for submarine landslides, and thus the tests described here are not strictly relevant to our own use of the model in NTHMP context. However, the model is increasingly being used to simulate the entire sequence of generation, propagation and inundation for events in confined regions such as fjords (Kirby et al, 2016) and the use of NTHMP benchmarks is thus relevant to establishing the general usability of the code in settings which may become of interest in future NTHMP activities.

A brief description to the NHWAVE model and its numerical implementation is given in Sections 2 and 3. In Section 4, the model is tested against standard NTHMP inundation benchmarks taken from Synolakis et al (2007) and mandated for the NTHMP Inundation Modeling Benchmark Workshop and subsequent inundation model validation. In this problem set, we have substituted the Monai Valley laboratory inundation test in place of the normally required Okishiri Island field data, as performing the Okishiri Island test with horizontal grid resolution needed to obtain accurate results would have been prohibitively time consuming, and is well outside the scope of present or anticipated uses of the code. Finally, results for benchmark tests required for the 2015 NTHMP Current Modeling Benchmark Workshop (Lynett et al, 2016) are described in Section 5. Derakhti et al (2016b,c) have provided further examples of the model's application to breaking of short wind waves, and have shown that the model properly describes the transformation of wave crests and development of turbulent bore features during depth-limited breaking, as seen in tsunami events.

2 Model description

An overview of the model formulation and numerical implementation follows. Readers are referred to Ma et al (2012) and Derakhti et al (2016a,b,c) for additional details of model development and testing.

2.1 Navier-Stokes equations

The incompressible Navier-Stokes equations in Cartesian coordinates (x_1^*, x_2^*, x_3^*) , where $x_1^* = x^*$, $x_2^* = y^*$ and $x_3^* = z^*$ and time t^* are given by

$$\frac{\partial u_i}{\partial x_i^*} = 0 \quad (1)$$

$$\frac{\partial u_i}{\partial t^*} + u_j \frac{\partial u_i}{\partial x_j^*} = -\frac{1}{\rho} \frac{\partial \tilde{p}}{\partial x_i^*} + g_i + \frac{\partial \tau_{ij}}{\partial x_j^*} \quad (2)$$

where $(i, j) = 1, 2, 3$, u_i is velocity component in the x_i^* direction, \tilde{p} is total pressure, ρ is water density, $g_i = -g\delta_{i3}$ is the gravitational body force and $\tau_{ij} = (\nu + \nu_t)(\partial u_i/\partial x_j^* + \partial u_j/\partial x_i^*)$ is turbulent stress with ν the molecular kinematic viscosity and ν_t the turbulent kinematic viscosity. Equations (1) and (2) are augmented by kinematic constraints given at the surface and bottom boundaries given by

$$\frac{\partial \eta}{\partial t^*} + u \frac{\partial \eta}{\partial x^*} + v \frac{\partial \eta}{\partial y^*} = w; \quad z^* = \eta \quad (3)$$

$$\frac{\partial h}{\partial t^*} + u \frac{\partial h}{\partial x^*} + v \frac{\partial h}{\partial y^*} = -w; \quad z^* = -h \quad (4)$$

where η and h are single valued functions of (x^*, y^*, t^*) , and by appropriate dynamic constraints described below.

2.2 Governing equations in σ coordinate system

In order to accurately represent bottom and surface geometry, a σ coordinate transformation developed by Phillips (1957) is used in NHWAVE. The coordinate transformation maps the bottom and surface onto constant boundaries of a strip of unit thickness. The transformation is given by

$$t = t^* \quad x = x^* \quad y = y^* \quad \sigma = \frac{z^* + h}{D} \quad (5)$$

where $D = h + \eta$. Using the chain rule, the partial derivatives of a variable $f = f(x^*, y^*, z^*, t^*)$ in the physical domain are transformed as follows.

$$\begin{aligned}\frac{\partial f}{\partial t^*} &= \frac{\partial f}{\partial t} + \frac{\partial f}{\partial \sigma} \frac{\partial \sigma}{\partial t^*} \\ \frac{\partial f}{\partial x^*} &= \frac{\partial f}{\partial x} + \frac{\partial f}{\partial \sigma} \frac{\partial \sigma}{\partial x^*} \\ \frac{\partial f}{\partial y^*} &= \frac{\partial f}{\partial y} + \frac{\partial f}{\partial \sigma} \frac{\partial \sigma}{\partial y^*} \\ \frac{\partial f}{\partial z^*} &= \frac{\partial f}{\partial \sigma} \frac{\partial \sigma}{\partial z^*}\end{aligned}\tag{6}$$

We obtain the governing equations in the new coordinate system (x, y, σ, t) using (5-6) in (1) and (2). The continuity equation (1) is first transformed as

$$\frac{\partial u}{\partial x} + \frac{\partial u}{\partial \sigma} \frac{\partial \sigma}{\partial x^*} + \frac{\partial v}{\partial y} + \frac{\partial v}{\partial \sigma} \frac{\partial \sigma}{\partial y^*} + \frac{1}{D} \frac{\partial w}{\partial \sigma} = 0\tag{7}$$

Using the results

$$\begin{aligned}\frac{\partial \sigma}{\partial t^*} &= \frac{1}{D} \frac{\partial h}{\partial t} - \frac{\sigma}{D} \frac{\partial D}{\partial t} \\ \frac{\partial \sigma}{\partial x^*} &= \frac{1}{D} \frac{\partial h}{\partial x} - \frac{\sigma}{D} \frac{\partial D}{\partial x} \\ \frac{\partial \sigma}{\partial y^*} &= \frac{1}{D} \frac{\partial h}{\partial y} - \frac{\sigma}{D} \frac{\partial D}{\partial y} \\ \frac{\partial \sigma}{\partial z^*} &= \frac{1}{D}\end{aligned}\tag{8}$$

we rewrite (7) as

$$\frac{\partial D}{\partial t} + \frac{\partial Du}{\partial x} + \frac{\partial Dv}{\partial y} + \frac{\partial \omega}{\partial \sigma} = 0\tag{9}$$

where ω is the vertical velocity relative to constant σ surfaces, given by

$$\omega = D \left(\frac{\partial \sigma}{\partial t^*} + u \frac{\partial \sigma}{\partial x^*} + v \frac{\partial \sigma}{\partial y^*} + w \frac{\partial \sigma}{\partial z^*} \right)\tag{10}$$

The transformed continuity equation (9) may be integrated over depth to obtain

$$\frac{\partial D}{\partial t} + \frac{\partial}{\partial x} \left(D \int_0^1 u d\sigma \right) + \frac{\partial}{\partial y} \left(D \int_0^1 v d\sigma \right) = 0\tag{11}$$

where the kinematic constraints (3) - (4) have been used. Equation (11) is used subsequently to determine the surface position.

The transformed momentum equations may be written as

$$\frac{\partial \mathbf{U}}{\partial t} + \frac{\partial \mathbf{F}}{\partial x} + \frac{\partial \mathbf{G}}{\partial y} + \frac{\partial \mathbf{H}}{\partial \sigma} = \mathbf{S}_h + \mathbf{S}_p + \mathbf{S}_\tau \quad (12)$$

where $\mathbf{U} = (Du, Dv, Dw)^T$. The fluxes are given by

$$\mathbf{F} = \begin{pmatrix} Duv + \frac{1}{2}gD^2 \\ Duv \\ Duv \end{pmatrix} \quad \mathbf{G} = \begin{pmatrix} Duv \\ Dvv + \frac{1}{2}gD^2 \\ Dvw \end{pmatrix} \quad \mathbf{H} = \begin{pmatrix} u\omega \\ v\omega \\ w\omega \end{pmatrix} \quad (13)$$

The source terms used here represent the effect of bottom slope on the hydrostatic pressure balance, the effect of the dynamic (nonhydrostatic) component of pressure, and the effect of turbulent stresses, and are given by

$$\mathbf{S}_h = \begin{pmatrix} gD \frac{\partial h}{\partial x} \\ gD \frac{\partial h}{\partial y} \\ 0 \end{pmatrix} \quad \mathbf{S}_p = \begin{pmatrix} -\frac{D}{\rho} \left(\frac{\partial p}{\partial x} + \frac{\partial p}{\partial \sigma} \frac{\partial \sigma}{\partial x^*} \right) \\ -\frac{D}{\rho} \left(\frac{\partial p}{\partial y} + \frac{\partial p}{\partial \sigma} \frac{\partial \sigma}{\partial y^*} \right) \\ -\frac{1}{\rho} \frac{\partial p}{\partial \sigma} \end{pmatrix} \quad \mathbf{S}_\tau = \begin{pmatrix} DS_{\tau_x} \\ DS_{\tau_y} \\ DS_{\tau_z} \end{pmatrix} \quad (14)$$

where the total pressure $\tilde{p} = p + \rho g(\eta - z^*)$ has been divided into its dynamic (p) and hydrostatic ($\rho g(\eta - z^*)$) parts, and turbulent diffusion terms $S_{\tau_x}, S_{\tau_y}, S_{\tau_z}$ are given by

$$\begin{aligned} S_{\tau_x} &= \frac{\partial \tau_{xx}}{\partial x} + \frac{\partial \tau_{xx}}{\partial \sigma} \frac{\partial \sigma}{\partial x^*} + \frac{\partial \tau_{xy}}{\partial y} + \frac{\partial \tau_{xy}}{\partial \sigma} \frac{\partial \sigma}{\partial y^*} + \frac{\partial \tau_{xz}}{\partial \sigma} \frac{\partial \sigma}{\partial z^*} \\ S_{\tau_y} &= \frac{\partial \tau_{yx}}{\partial x} + \frac{\partial \tau_{yx}}{\partial \sigma} \frac{\partial \sigma}{\partial x^*} + \frac{\partial \tau_{yy}}{\partial y} + \frac{\partial \tau_{yy}}{\partial \sigma} \frac{\partial \sigma}{\partial y^*} + \frac{\partial \tau_{yz}}{\partial \sigma} \frac{\partial \sigma}{\partial z^*} \\ S_{\tau_z} &= \frac{\partial \tau_{zx}}{\partial x} + \frac{\partial \tau_{zx}}{\partial \sigma} \frac{\partial \sigma}{\partial x^*} + \frac{\partial \tau_{zy}}{\partial y} + \frac{\partial \tau_{zy}}{\partial \sigma} \frac{\partial \sigma}{\partial y^*} + \frac{\partial \tau_{zz}}{\partial \sigma} \frac{\partial \sigma}{\partial z^*} \end{aligned} \quad (15)$$

Stresses in the transformed σ coordinates are given by

$$\begin{aligned} \tau_{xx} &= 2(\nu + \nu_t) \left(\frac{\partial u}{\partial x} + \frac{\partial u}{\partial \sigma} \frac{\partial \sigma}{\partial x^*} \right) & \tau_{xy} = \tau_{yx} &= (\nu + \nu_t) \left(\frac{\partial u}{\partial y} + \frac{\partial u}{\partial \sigma} \frac{\partial \sigma}{\partial y^*} + \frac{\partial v}{\partial x} + \frac{\partial v}{\partial \sigma} \frac{\partial \sigma}{\partial x^*} \right) \\ \tau_{yy} &= 2(\nu + \nu_t) \left(\frac{\partial v}{\partial y} + \frac{\partial v}{\partial \sigma} \frac{\partial \sigma}{\partial y^*} \right) & \tau_{xz} = \tau_{zx} &= (\nu + \nu_t) \left(\frac{\partial u}{\partial \sigma} \frac{\partial \sigma}{\partial z^*} + \frac{\partial w}{\partial x} + \frac{\partial w}{\partial \sigma} \frac{\partial \sigma}{\partial x^*} \right) \\ \tau_{zz} &= 2(\nu + \nu_t) \left(\frac{\partial w}{\partial \sigma} \frac{\partial \sigma}{\partial z^*} \right) & \tau_{yz} = \tau_{zy} &= \nu_t \left(\frac{\partial v}{\partial \sigma} \frac{\partial \sigma}{\partial z^*} + \frac{\partial w}{\partial y} + \frac{\partial w}{\partial \sigma} \frac{\partial \sigma}{\partial y^*} \right) \end{aligned} \quad (16)$$

It has been noted in a number of previous studies that the application of standard finite volume Godunov-type scheme directly to equations of this form does not lead to an automatic preservation of steady state (Zhou et al, 2001; Kim et al, 2008; Liang and Marche, 2009). Therefore, It is desirable to reformulate the equations so that the flux and source terms can be automatically balanced at the discrete level in the steady state. Following Shi et al (2011), the source term is rewritten as

$$g(h + \eta) \frac{\partial h}{\partial x} = \frac{\partial}{\partial x} \left(\frac{1}{2}gh^2 \right) + g\eta \frac{\partial h}{\partial x} \quad (17)$$

in which the first term in the right hand side can be combined together with the flux terms. Based on this, the flux terms \mathbf{F} and \mathbf{G} and source term \mathbf{S}_h are rewritten as

$$\mathbf{F} = \begin{pmatrix} Duv + \frac{1}{2}g\eta^2 + gh\eta \\ Duv \\ Duv \end{pmatrix} \quad \mathbf{G} = \begin{pmatrix} Duv \\ Dvv + \frac{1}{2}g\eta^2 + gh\eta \\ Dvv \end{pmatrix} \quad \mathbf{S}_h = \begin{pmatrix} g\eta \frac{\partial h}{\partial x} \\ g\eta \frac{\partial h}{\partial y} \\ 0 \end{pmatrix} \quad (18)$$

The main advantage of the above formulation is that the flux and source terms are well-balanced so that no artificial flow due to bottom slope will be generated.

2.3 Turbulence Model

The turbulent kinematic viscosity ν_t in (16) can be estimated by the Smagorinsky subgrid model (as is typical for LES simulations) or the $k-\epsilon$ turbulence closure. This choice is made by the user as part of the input data.

The Smagorinsky subgrid model is expressed as

$$\nu_t = (C_s \Delta)^2 \sqrt{2S_{ij}S_{ij}} \quad (19)$$

where C_s is the Smagorinsky coefficient, which is taken as 0.1~0.2, Δ is the filter width, which is calculated as $\Delta = (\Delta x \Delta y \Delta \sigma D)^{1/3}$, and $S_{ij} = \frac{1}{2}(\frac{\partial u_i}{\partial x_j^*} + \frac{\partial u_j}{\partial x_i^*})$ is the stress tensor.

We have also implemented a nonlinear $k-\epsilon$ model into NHWAVE to simulate turbulent flow. The turbulent eddy viscosity is calculated by

$$\nu_t = C_\mu \frac{k^2}{\epsilon} \quad (20)$$

When taking into account free surface and bottom slopes (Derakhti et al, 2016a), the $k-\epsilon$ equations in conservative form are given by

$$\begin{aligned} \frac{\partial Dk}{\partial t} + \nabla \cdot (D\mathbf{u}k) &= \nabla_h \cdot \left[\nu^k \left(\nabla(Dk) + \frac{\partial((\sigma_x^* + \sigma_y^*)Dk)}{\partial \sigma} \right) \right] \\ &+ \frac{\partial}{\partial \sigma} \left[\nu^k \left(\nabla_s(Dk) + \frac{\partial((\sigma_x^{*2} + \sigma_y^{*2})Dk)}{\partial \sigma} \right) \right] + D(P_s + P_b - \epsilon) \end{aligned} \quad (21)$$

$$\begin{aligned} \frac{\partial D\epsilon}{\partial t} + \nabla \cdot (D\mathbf{u}\epsilon) &= \nabla_h \cdot \left[\nu^\epsilon \left(\nabla(D\epsilon) + \frac{\partial((\sigma_x^* + \sigma_y^*)D\epsilon)}{\partial \sigma} \right) \right] \\ &+ \frac{\partial}{\partial \sigma} \left[\nu^\epsilon \left(\nabla_s(D\epsilon) + \frac{\partial((\sigma_x^{*2} + \sigma_y^{*2})D\epsilon)}{\partial \sigma} \right) \right] + \frac{\epsilon}{k} D(C_{1\epsilon}(P_s + C_{3\epsilon}P_b) - C_{2\epsilon}\epsilon) \end{aligned} \quad (22)$$

where $\nu^k = \nu + \nu_t/\sigma_k$, $\nu^\epsilon = \nu + \nu_t/\sigma_\epsilon$, ∇_h is horizontal divergence, operator $\nabla_s = \sigma_x^* \partial/\partial x + \sigma_y^* \partial/\partial y + \partial/\partial \sigma$, and $C_{3\epsilon} = 0$.

2.3.1 Standard $k - \epsilon$.

In the standard $k - \epsilon$ model, we have (Lin and Liu, 1998)

$$\sigma_k = 1.0, \quad \sigma_\epsilon = 1.3, \quad C_{1\epsilon} = 1.44, \quad C_{2\epsilon} = 1.92, \quad C_\mu = 0.09 \quad (23)$$

2.3.2 Renormalization Group (RNG) $k - \epsilon$.

The RNG approach employs scale expansions for the Reynolds stress and production of dissipation terms. Yakhot et al (1992) derived a dynamic procedure to determine $C_{2\epsilon}$, which is then given by

$$C_{2\epsilon} = 1.68 + \frac{c_\mu \zeta^3 (1 - \zeta/4.38)}{1 + 0.012 \zeta^3}, \quad (24)$$

where $\zeta = \frac{k}{\epsilon} \sqrt{2S_{ij}S_{ij}}$ is the ratio of the turbulent and mean strain time scales. The rest of the closure coefficients are given by

$$C_\mu = 0.085, \quad C_{1\epsilon} = 1.42, \quad \sigma_k = 0.72, \quad \sigma_\epsilon = 0.72. \quad (25)$$

Finally, the production rates for shear, P_s , and buoyancy, P_b , are given by

$$P_s = -\overline{u'_i u'_j} \frac{\partial u_i}{\partial x_j^*} \quad (26)$$

and

$$P_b = \frac{g}{\rho_0} \frac{\nu_t}{D} \frac{\partial \rho_m}{\partial \sigma} \quad (27)$$

where the Reynolds stress $\overline{u'_i u'_j}$ is calculated by a nonlinear model proposed by Lin and Liu (1998), which is given by

$$\begin{aligned} \overline{u'_i u'_j} = & -C_d \frac{k^2}{\epsilon} \left(\frac{\partial u_i}{\partial x_j^*} + \frac{\partial u_j}{\partial x_i^*} \right) + \frac{2}{3} k \delta_{ij} \\ & - C_1 \frac{k^3}{\epsilon^2} \left(\frac{\partial u_i}{\partial x_l^*} \frac{\partial u_l}{\partial x_j^*} + \frac{\partial u_j}{\partial x_l^*} \frac{\partial u_l}{\partial x_i^*} - \frac{2}{3} \frac{\partial u_l}{\partial x_k^*} \frac{\partial u_k}{\partial x_l^*} \delta_{ij} \right) \\ & - C_2 \frac{k^3}{\epsilon^2} \left(\frac{\partial u_i}{\partial x_k^*} \frac{\partial u_j}{\partial x_k^*} - \frac{1}{3} \frac{\partial u_l}{\partial x_k^*} \frac{\partial u_l}{\partial x_k^*} \delta_{ij} \right) \\ & - C_3 \frac{k^3}{\epsilon^2} \left(\frac{\partial u_k}{\partial x_i^*} \frac{\partial u_k}{\partial x_j^*} - \frac{1}{3} \frac{\partial u_l}{\partial x_k^*} \frac{\partial u_l}{\partial x_k^*} \delta_{ij} \right) \end{aligned} \quad (28)$$

where C_d , C_1 , C_2 and C_3 are empirical coefficients as given by Lin and Liu (1998)

$$\begin{aligned} C_d = \frac{2}{3} \left(\frac{1}{7.4 + 2S_{max}} \right), \quad C_1 = \frac{1}{185.2 + 3D_{max}^2} \\ C_2 = -\frac{1}{58.5 + 2D_{max}^2}, \quad C_3 = \frac{1}{370.4 + 3D_{max}^2} \end{aligned} \quad (29)$$

where

$$\begin{aligned}
S_{max} &= \frac{k}{\epsilon} \max \left\{ \left| \frac{\partial u_i}{\partial x_i^*} \right| \right\} \text{ (indices not summed)} \\
D_{max} &= \frac{k}{\epsilon} \max \left\{ \left| \frac{\partial u_i}{\partial x_j^*} \right| \right\}
\end{aligned} \tag{30}$$

The coefficients here ensure the non-negativity of turbulent velocities and bounded Reynolds stress. They have been successfully applied to simulate breaking waves on plane beaches (Lin and Liu, 1998, Derakhti et al, 2016b,c).

3 Numerical method

3.1 Grid configuration

A combined finite-volume and finite-difference scheme with a Godunov-type method was applied to discretize equations (9) and (12). It is straightforward to define all dependent variables at cell centers to solve the Riemann problem. However, this treatment results in checkerboard solutions in which the pressure and velocity become decoupled when they are defined at the same location (Patankar, 1980). Therefore, most existing models use a staggered grid in which the pressure is defined at the centers of computational cells and the velocities are defined at cell faces (Bradford, 2005). However, staggered grids do not lend themselves as easily as co-located grids to the use of Godunov-type schemes. Meanwhile, difficulty in treating the cell-centered pressure at the top layer may arise when applying the pressure boundary condition at the free surface (Yuan and Wu, 2004).

With these considerations, a different kind of staggered grid framework is introduced, in which the velocities are placed at the cell centers and the pressure is defined at the vertically-facing cell faces as shown in figure 1. The momentum equations are solved by a second-order Godunov-type finite volume method. The HLL approximate Riemann solver (Harten et al, 1983) is used to estimate fluxes at the cell faces. As in Stelling and Zijlema (2003), the pressure boundary condition at the free surface can be precisely assigned to zero.

3.2 Time Stepping

To obtain second-order temporal accuracy, the two-stage second-order nonlinear Strong Stability-Preserving (SSP) Runge-Kutta scheme (Gottlieb et al, 2001) is adopted for time stepping. At the first stage, an intermediate quantity $\mathbf{U}^{(1)}$ is evaluated using a typical first-order, two-step projection method given by

$$\frac{\mathbf{U}^* - \mathbf{U}^n}{\Delta t} = - \left(\frac{\partial \mathbf{F}}{\partial x} + \frac{\partial \mathbf{G}}{\partial y} + \frac{\partial \mathbf{H}}{\partial \sigma} \right)^n + \mathbf{S}_h^n + \mathbf{S}_\tau^n \tag{31}$$

$$\frac{\mathbf{U}^{(1)} - \mathbf{U}^*}{\Delta t} = \mathbf{S}_p^{(1)} \tag{32}$$

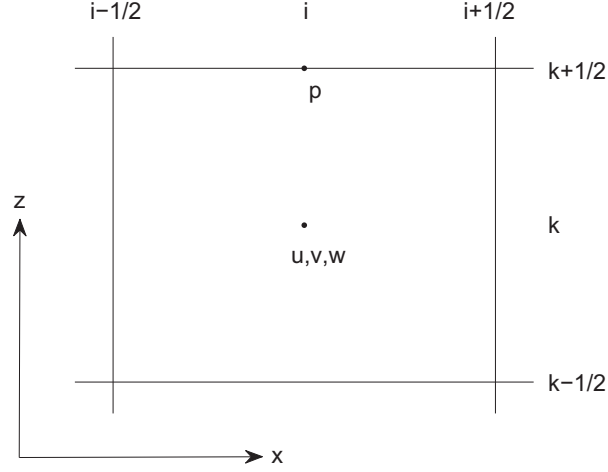


Figure 1: Layout of computational variables. Velocities (u, v, w) are placed at cell center and dynamic pressure p is defined at vertical cell face.

where \mathbf{U}^n represents \mathbf{U} value at time level n , \mathbf{U}^* is the intermediate value in the two-step projection method, and $\mathbf{U}^{(1)}$ is the final first stage estimate. In the second stage, the velocity field is again updated to a second intermediate level using the same projection method, after which the Runge-Kutta algorithm is used to obtain a final value of the solution at the $n + 1$ time level.

$$\frac{\mathbf{U}^* - \mathbf{U}^{(1)}}{\Delta t} = - \left(\frac{\partial \mathbf{F}}{\partial x} + \frac{\partial \mathbf{G}}{\partial y} + \frac{\partial \mathbf{H}}{\partial \sigma} \right)^{(1)} + \mathbf{S}_h^{(1)} + \mathbf{S}_\tau^{(1)} \quad (33)$$

$$\frac{\mathbf{U}^{(2)} - \mathbf{U}^*}{\Delta t} = \mathbf{S}_p^{(2)} \quad (34)$$

$$\mathbf{U}^{n+1} = \frac{1}{2} \mathbf{U}^n + \frac{1}{2} \mathbf{U}^{(2)} \quad (35)$$

Each stage of the calculation requires the specification of the nonhydrostatic component of the pressure force as expressed through the quantities $\mathbf{S}_p^{(1,2)}$. The pressure field needed to specify these is based on the solution of the Poisson equation described below. Also at each stage, the surface elevation is obtained by solving equation (11) explicitly. The time step Δt is adaptive during the simulation, following the Courant-Friedrichs-Lewy (CFL) criterion

$$\Delta t = C \min \left[\min \frac{\Delta x}{|u_{i,j,k}| + \sqrt{gD_{i,j}}}, \min \frac{\Delta y}{|v_{i,j,k}| + \sqrt{gD_{i,j}}}, \min \frac{\Delta \sigma D_{i,j}}{|w_{i,j,k}|} \right] \quad (36)$$

where C is the Courant number, which is taken to be 0.5 to ensure accuracy and stability in the current model.

3.3 Spatial finite volume scheme

Equation (9) and (12) are discretized using a second-order Godunov-type finite volume method. To solve equation (9) and (12), fluxes based on the conservative variables are required at the cell faces. In high-order Godunov-type methods, the values of the conservative variables within a cell are calculated using a reconstruction method based on the cell center data (Zhou et al, 2001). Usually a piecewise linear reconstruction is used, leading to a second order scheme. For \mathbf{U} in the cell i , we have

$$\mathbf{U} = \mathbf{U}_i + (x - x_i)\Delta\mathbf{U}_i \quad (37)$$

where $\Delta\mathbf{U}_i$ is the gradient of \mathbf{U} , which is calculated by

$$\Delta\mathbf{U}_i = \text{avg} \left(\frac{\mathbf{U}_{i+1} - \mathbf{U}_i}{x_{i+1} - x_i}, \frac{\mathbf{U}_i - \mathbf{U}_{i-1}}{x_i - x_{i-1}} \right) \quad (38)$$

in which avg is a slope limiter which is used to avoid spurious oscillations in the reconstruction data at the cell faces. In NHWAVE, the van Leer limiter is adopted, which is given by

$$\text{avg}(a, b) = \frac{a|b| + |a|b}{|a| + |b|} \quad (39)$$

The left and right values of \mathbf{U} at cell face $(i + \frac{1}{2})$ are given by

$$\mathbf{U}_{i+\frac{1}{2}}^L = \mathbf{U}_i + \frac{1}{2}\Delta x_i \Delta\mathbf{U}_i \quad \mathbf{U}_{i+\frac{1}{2}}^R = \mathbf{U}_{i+1} - \frac{1}{2}\Delta x_{i+1} \Delta\mathbf{U}_{i+1} \quad (40)$$

The flux $\mathbf{F}(\mathbf{U}^L, \mathbf{U}^R)$ is calculated by solving a local Riemann problem at each horizontally-facing cell face. In the present study, the HLL approximate Riemann solver is employed. The flux at the cell interface $(i + \frac{1}{2})$ is determined by

$$\mathbf{F}(\mathbf{U}^L, \mathbf{U}^R) = \begin{cases} \mathbf{F}(\mathbf{U}^L) & \text{if } s_L \geq 0 \\ \mathbf{F}^*(\mathbf{U}^L, \mathbf{U}^R) & \text{if } s_L < 0 < s_R \\ \mathbf{F}(\mathbf{U}^R) & \text{if } s_R \leq 0 \end{cases} \quad (41)$$

where

$$\mathbf{F}^*(\mathbf{U}^L, \mathbf{U}^R) = \frac{s_R \mathbf{F}(\mathbf{U}^L) - s_L \mathbf{F}(\mathbf{U}^R) + s_L s_R (\mathbf{U}^R - \mathbf{U}^L)}{s_R - s_L} \quad (42)$$

with wave speed s_L and s_R defined by

$$s_L = \min(u^L - \sqrt{gD_L}, u_s - \sqrt{gD_s}) \quad (43)$$

$$s_R = \max(u^R + \sqrt{gD_R}, u_s + \sqrt{gD_s}) \quad (44)$$

where u_s and $\sqrt{gD_s}$ are estimated by

$$u_s = \frac{1}{2}(u^L + u^R) + \sqrt{gD_L} - \sqrt{gD_R} \quad (45)$$

$$\sqrt{gD_s} = \frac{\sqrt{gD_L} + \sqrt{gD_R}}{2} + \frac{u^L - u^R}{4} \quad (46)$$

To obtain the non-hydrostatic velocity field, the dynamic pressure p has to be calculated first. From equation (32) and (34), we get

$$u^{(k)} = u^* - \frac{\Delta t}{\rho} \left(\frac{\partial p}{\partial x} + \frac{\partial p}{\partial \sigma} \frac{\partial \sigma}{\partial x^*} \right)^{(k)} \quad (47)$$

$$v^{(k)} = v^* - \frac{\Delta t}{\rho} \left(\frac{\partial p}{\partial y} + \frac{\partial p}{\partial \sigma} \frac{\partial \sigma}{\partial y^*} \right)^{(k)} \quad (48)$$

$$w^{(k)} = w^* - \frac{\Delta t}{\rho} \frac{1}{D^{(k)}} \frac{\partial p^{(k)}}{\partial \sigma} \quad (49)$$

where $k = 1, 2$ represents the k th stage in the Runge-Kutta integration.

Substituting equation (47) - (49) into the continuity equation (7), we obtain the Poisson equation in (x, y, σ) coordinate system, given by

$$\begin{aligned} & \frac{\partial}{\partial x} \left[\frac{\partial p}{\partial x} + \frac{\partial p}{\partial \sigma} \frac{\partial \sigma}{\partial x^*} \right] + \frac{\partial}{\partial y} \left[\frac{\partial p}{\partial y} + \frac{\partial p}{\partial \sigma} \frac{\partial \sigma}{\partial y^*} \right] + \frac{\partial}{\partial \sigma} \left(\frac{\partial p}{\partial x} \right) \frac{\partial \sigma}{\partial x^*} + \\ & \frac{\partial}{\partial \sigma} \left(\frac{\partial p}{\partial y} \right) \frac{\partial \sigma}{\partial y^*} + \left[\left(\frac{\partial \sigma}{\partial x^*} \right)^2 + \left(\frac{\partial \sigma}{\partial y^*} \right)^2 + \frac{1}{D^2} \right] \frac{\partial}{\partial \sigma} \left(\frac{\partial p}{\partial \sigma} \right) = \\ & \frac{\rho}{\Delta t} \left(\frac{\partial u^*}{\partial x} + \frac{\partial u^*}{\partial \sigma} \frac{\partial \sigma}{\partial x^*} + \frac{\partial v^*}{\partial y} + \frac{\partial v^*}{\partial \sigma} \frac{\partial \sigma}{\partial y^*} + \frac{1}{D} \frac{\partial w^*}{\partial \sigma} \right) \end{aligned} \quad (50)$$

The above equation is discretized using second-order space-centered finite differences. The velocities (u^*, v^*, w^*) at vertical cell faces are interpolated from adjacent cell-centered values. The resulting linear equation is given by

$$\begin{aligned} & a_1 p_{i,j-1,k-1} + a_2 p_{i-1,j,k-1} + a_3 p_{i,j,k-1} + a_4 p_{i+1,j,k-1} + a_5 p_{i,j+1,k-1} + \\ & a_6 p_{i,j-1,k} + a_7 p_{i-1,j,k} + a_8 p_{i,j,k} + a_9 p_{i+1,j,k} + a_{10} p_{i,j+1,k} + a_{11} p_{i,j-1,k+1} + \\ & a_{12} p_{i-1,j,k+1} + a_{13} p_{i,j,k+1} + a_{14} p_{i+1,j,k+1} + a_{15} p_{i,j+1,k+1} = R_p \end{aligned} \quad (51)$$

where

$$\begin{aligned} a_1 &= - \left(\frac{(\sigma_y)_{i,j-1,k}}{2\Delta y(\Delta\sigma_k + \Delta\sigma_{k-1})} + \frac{(\sigma_y)_{i,j,k}}{2\Delta y(\Delta\sigma_k + \Delta\sigma_{k-1})} \right) \\ a_2 &= - \left(\frac{(\sigma_x)_{i-1,j,k}}{2\Delta x(\Delta\sigma_k + \Delta\sigma_{k-1})} + \frac{(\sigma_x)_{i,j,k}}{2\Delta x(\Delta\sigma_k + \Delta\sigma_{k-1})} \right) \\ a_3 &= - \frac{(\sigma_x^2 + \sigma_y^2 + \frac{1}{D^2})_{i,j,k}}{0.5(\Delta\sigma_k + \Delta\sigma_{k-1})\Delta\sigma_{k-1}} \\ a_4 &= \frac{(\sigma_x)_{i+1,j,k}}{2\Delta x(\Delta\sigma_k + \Delta\sigma_{k-1})} + \frac{(\sigma_x)_{i,j,k}}{2\Delta x(\Delta\sigma_k + \Delta\sigma_{k-1})} \\ a_5 &= \frac{(\sigma_y)_{i,j+1,k}}{2\Delta y(\Delta\sigma_k + \Delta\sigma_{k-1})} + \frac{(\sigma_y)_{i,j,k}}{2\Delta y(\Delta\sigma_k + \Delta\sigma_{k-1})} \end{aligned}$$

$$\begin{aligned}
a_6 &= a_{10} = -\frac{1}{\Delta y^2} & a_7 &= a_9 = -\frac{1}{\Delta x^2} \\
a_8 &= \frac{2}{\Delta x^2} + \frac{2}{\Delta y^2} + \frac{(\sigma_x^2 + \sigma_y^2 + \frac{1}{D^2})_{i,j,k}}{0.5(\Delta\sigma_k + \Delta\sigma_{k-1})\Delta\sigma_k} + \frac{(\sigma_x^2 + \sigma_y^2 + \frac{1}{D^2})_{i,j,k}}{0.5(\Delta\sigma_k + \Delta\sigma_{k-1})\Delta\sigma_{k-1}} \\
a_{11} &= \frac{(\sigma_y)_{i,j-1,k}}{2\Delta y(\Delta\sigma_k + \Delta\sigma_{k-1})} + \frac{(\sigma_y)_{i,j,k}}{2\Delta y(\Delta\sigma_k + \Delta\sigma_{k-1})} \\
a_{12} &= \frac{(\sigma_x)_{i-1,j,k}}{2\Delta x(\Delta\sigma_k + \Delta\sigma_{k-1})} + \frac{(\sigma_x)_{i,j,k}}{2\Delta x(\Delta\sigma_k + \Delta\sigma_{k-1})} \\
a_{13} &= -\frac{(\sigma_x^2 + \sigma_y^2 + \frac{1}{D^2})_{i,j,k}}{0.5(\Delta\sigma_k + \Delta\sigma_{k-1})\Delta\sigma_k} \\
a_{14} &= -\left(\frac{(\sigma_x)_{i+1,j,k}}{2\Delta x(\Delta\sigma_k + \Delta\sigma_{k-1})} + \frac{(\sigma_x)_{i,j,k}}{2\Delta x(\Delta\sigma_k + \Delta\sigma_{k-1})} \right) \\
a_{15} &= -\left(\frac{(\sigma_y)_{i,j+1,k}}{2\Delta y(\Delta\sigma_k + \Delta\sigma_{k-1})} + \frac{(\sigma_y)_{i,j,k}}{2\Delta y(\Delta\sigma_k + \Delta\sigma_{k-1})} \right) \\
R_p &= -\frac{\rho}{\Delta t} \left(\frac{\partial u^*}{\partial x} + \frac{\partial u^*}{\partial \sigma} \frac{\partial \sigma}{\partial x^*} + \frac{\partial v^*}{\partial y} + \frac{\partial v^*}{\partial \sigma} \frac{\partial \sigma}{\partial y^*} + \frac{1}{D} \frac{\partial w^*}{\partial \sigma} \right)
\end{aligned}$$

where $\sigma_x = \frac{\partial \sigma}{\partial x^*}$ and $\sigma_y = \frac{\partial \sigma}{\partial y^*}$.

Uniform gridding is used in the horizontal direction while gridding in the vertical direction is generalized to be non-uniform in order to capture the bottom and surface boundary layers when desired. The coefficient matrix is asymmetric and has a total of 15 diagonal lines. The linear system is solved using the high performance preconditioner HYPRE software library. With p solved, the non-hydrostatic velocities at each stage can be updated from equation (47) to (49).

3.4 Boundary conditions

Assuming no mass flux at the interface, the kinematic surface and bottom boundary conditions in the σ -coordinate system are simply written as

$$w \Big|_{\sigma=0,1} = \xi_t + \xi_x u \Big|_{\sigma=0,1} + \xi_y v \Big|_{\sigma=0,1} \quad (52)$$

where $\xi = \eta$ at the free surface ($\sigma = 1$), and $\xi = -h$ at the bottom ($\sigma = 0$).

Using the continuity of the tangential stress on the bottom and top boundaries ($\sigma = 0, 1$), Derakhti et al (2016a) showed that

$$\begin{aligned}
\frac{\partial u}{\partial \sigma} \Big|_{\sigma=0,1} &= \frac{D}{A\rho(\nu + \nu_t)} \mathcal{F}_1^{ext} \Big|_{\sigma=0,1} - \xi_x \frac{\partial w}{\partial \sigma} \Big|_{\sigma=0,1} \\
&+ \frac{D}{A^2} \left\{ 2\xi_x \frac{\partial u}{\partial x} - [1 - \xi_x^2] \frac{\partial w}{\partial x} + \xi_y \left[\frac{\partial u}{\partial y} + \frac{\partial v}{\partial x} + \xi_x \frac{\partial w}{\partial y} \right] \right\}_{\sigma=0,1} \\
\frac{\partial v}{\partial \sigma} \Big|_{\sigma=0,1} &= \frac{D}{A\rho(\nu + \nu_t)} \mathcal{F}_2^{ext} \Big|_{\sigma=0,1} - \xi_y \frac{\partial w}{\partial \sigma} \Big|_{\sigma=0,1} \\
&+ \frac{D}{A^2} \left\{ 2\xi_y \frac{\partial v}{\partial y} - [1 - \xi_y^2] \frac{\partial w}{\partial y} + \xi_x \left[\frac{\partial v}{\partial x} + \frac{\partial u}{\partial y} + \xi_y \frac{\partial w}{\partial x} \right] \right\}_{\sigma=0,1},
\end{aligned} \tag{53}$$

where $A = \sqrt{1 + \xi_x^2 + \xi_y^2}$, and \mathcal{F}_1^{ext} and \mathcal{F}_2^{ext} are the external tangential stress.

The external tangential stress at $\sigma = 1$ represents wind-induced shear stress, which is not employed in the present study: we use $\mathcal{F}_1^{ext} \Big|_{\sigma=1} = \mathcal{F}_2^{ext} \Big|_{\sigma=1} = 0$ in the entire numerical domain. The external shear stress near the bottom is approximated using the law of the wall, assuming a uniform bottom roughness height as in Derakhti et al (2016a).

Neglecting viscous stresses on the air side, the condition of no normal stress on the free surface leads to a Dirichlet-type boundary condition for the modified ensemble-averaged dynamic pressure at $\sigma = 1$ (Derakhti et al., 2016a)

$$\begin{aligned}
p \Big|_{\sigma=1} &= -\frac{\rho(\nu + \nu_t)}{A^2} \Big|_{\sigma=1} \left\{ 2\xi_x \left[\frac{\partial w}{\partial x} - \xi_x \frac{\partial u}{\partial x} \right] + 2\xi_y \left[\frac{\partial w}{\partial y} - \xi_y \frac{\partial v}{\partial y} \right] \right. \\
&\quad \left. - 2\xi_x \xi_y \left[\frac{\partial u}{\partial y} + \frac{\partial v}{\partial x} \right] \right\}_{\sigma=1}.
\end{aligned} \tag{54}$$

At the bottom, however, such a relation can not be applied unless the bottom is a dynamically coupled layer. By neglecting the Reynolds stress gradients at the bottom, a Neumann-type boundary condition for the modified dynamic pressure at the bottom is given by (Derakhti et al., 2016a)

$$\frac{\partial p}{\partial \sigma} \Big|_{\sigma=0} = -\rho \left\{ \frac{\partial Dw}{\partial t} + \frac{\partial D_{uw}}{\partial x} + \frac{\partial D_{vw}}{\partial y} \right\}_{\sigma=0}. \tag{55}$$

3.5 Basic hydrodynamic considerations

There are two basic states which are required in ensuring that any numerical model works for predicting evolution and inundations. The first step is to ensuring that the model conserves mass; the second basic step is checking convergence of this numerical code to a asymptotic limit.

3.5.1 Mass conservation

Conservation of mass can be checked by calculating water volume at the beginning and at the end of the computation. This should be done by integrating disturbed water depth $\eta(x, y, t)$ over the entire flow domain, i.e., if the flow domain extends from the maximum penetration during inundation $x = X_{max}$ to the outer location of the source region X_S , and $y = Y_{max}$ to Y_S , then the total displaced volume $V(t)$ is,

$$V(t) = \int_{X_{max}}^{X_S} \int_{Y_{max}}^{Y_S} \eta(x, y, t) dx dy \quad (56)$$

The integral of $\eta(x, y, t)$ should be used instead of the integral of the entire flow depth $h(x, y, t) = \eta(x, y, t) + d(x, y, t)$ where $d(x, y, t)$ is the undisturbed water depth, because the latter is likely to conceal errors in the calculation. Typically, $\eta \ll d$ at offshore integrating h will simply produce the entire volume of the flow domain and will mask errors. Note that testing of the conservation of mass as above involves placing a closed domain within reflective boundaries (Synolakis et al, 2007).

Calculations of conservation of mass has been done for all of the benchmark problems reviewed in this report such that the total initial displaced volume $V(t = 0)$ was within less than 1% of the total displaced volume at the end of the computation $V(t = T)$ where T represents the computation end time. It is assumed that the end of the computation is when the initial wave is entirely reflected and reached offshore. However, with few changes in Δx and Δy the conservation of mass can be improved.

3.5.2 Convergence

Convergence is the another basic hydrodynamic consideration that is checked for all of the benchmarks in this research. Actually this process is made by checking convergence of the numerical code to a certain asymptotic limit, presumably the actual solution of the equations solved. The grid steps Δx and Δy has been halved, and the time step Δt automatically reduced appropriately to conform to the Courant-Friedrichs-Levy (CFL) criterion. As recommended in literature, convergence of the code has been checked through the extreme runup and rundown. Table 1 displays convergence of the code tested for the analytical case of $H/d = 0.019$ solitary wave on a simple 1:19.85 beach which is discussed in Section 4.1 below, and Figure 2 shows the convergence rate of the case compared to 2nd-order rate.

Grid Size	Maximum Runup	Relative error(%)
0.2	0.07335	2.70
0.1	0.07471	0.89
0.05	0.07511	0.36
0.025	0.07539	0.00

Table 1: Maximum runup for analytical case of solitary wave on a simple beach with different grid size.

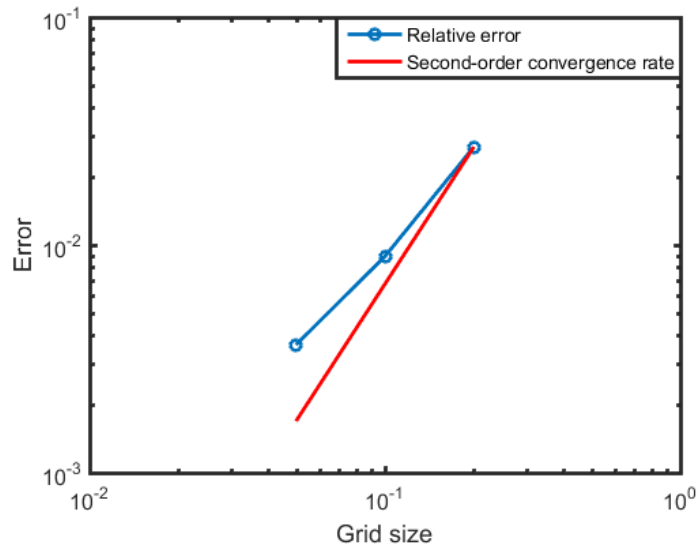


Figure 2: Convergence rate of the case.

4 Inundation benchmarks

In this section, one analytical benchmark and four laboratory benchmarks are studied as inundation benchmarks, and results of numerical calculations are compared to the data from Synolakis et al (2007). The following benchmark problems are studied in this section:

1. Solitary wave on a simple beach: analytical
2. Solitary wave on a simple beach: laboratory
3. Solitary wave on a conical island
4. Tsunami runup onto a complex 3-D beach; Monai Valley

4.1 Solitary wave on a simple beach: analytical

In this problem, we consider the non-breaking runup of a solitary wave on a plane slope. The test data is an analytic solution of the linear shallow water equations. Long waves climb a sloping beach of angle β attached to a constant-depth region (Figure 3). The origin of the coordinate system is at the initial position of the shoreline and x increases seaward.

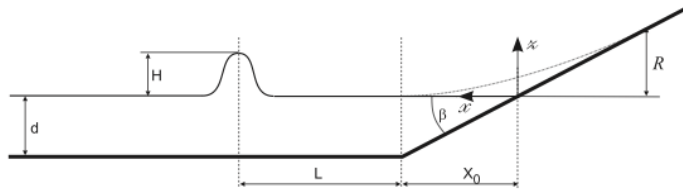


Figure 3: Definition sketch for simple beach bathymetry(from Synolakis et al (2007, Figure A1)).

It is possible to derive exact results for the evolution and runup of solitary waves based on linear theory (Synolakis, 1986, 1987). Solitary waves have long been used as a model for the leading wave of tsunamis. Russell (1845) defined solitary waves as the great waves of translation, and consists of a single elevation wave. While capturing some of the basic physics of tsunamis, solitary waves do not model the physical manifestation of tsunamis in nature, which are invariably N -wave like with a leading-depression wave followed by an elevation wave (Synolakis et al, 2007). The following runup law for the maximum runup R is provided based on slope of the beach and wave height of the solitary wave

$$R = 2.831 \sqrt{\cot \beta} (H/d)^{\frac{5}{4}} \quad (57)$$

Benchmark problems that are studied here have different depths of 0.5 and 5m, with different slopes and wave heights. Table 2 provides a list of selected examples that has been modeled including their maximum runup and the grid size for each case. All cases use 3 vertical cells and

turn off the option of viscous flow to better compare the analytical solutions. The model has no provision for running in a linear configuration. Figure 4 provides a comparison between numerical simulations and the runup law.

d(m)	Δx (m)	H/d	Cot (β)	R/d		
				Runup Law	Numerical Calculations	Error (%)
0.5	0.05	0.01	10.0	0.0283	0.0302	6.75
0.5	0.05	0.02	10.0	0.0673	0.0704	4.56
0.5	0.05	0.03	10.0	0.1118	0.1110	0.69
0.5	0.05	0.05	10.0	0.2117	0.2010	5.04
0.5	0.05	0.10	3.333	0.2906	0.2921	0.51
5	0.5	0.03	10.0	0.1118	0.1102	1.41
5	0.5	0.05	10.0	0.2117	0.2002	5.42
5	0.5	0.10	3.372	0.2923	0.3051	4.35
5	0.5	0.20	3.372	0.6953	0.6609	4.94

Table 2: Runup data from numerical calculations compared with runup law values.

In addition, the analytical solution for different times is available for a specific case in which $H/d = 0.019$ and $\beta = \cot^{-1}(19.85)$. In order to have the same time with the data it was recommended that $L = \cosh^{-1}(\sqrt{20})/\gamma$ in which $\gamma = \sqrt{3H/4d}$; therefore, the distance of the wave from initial shoreline(X_1) can be written as $X_1 = X_0 + L$ (with respect to Figure 3). Figure 5 demonstrates profiles and time series of the water in eight different times. Extreme positions of the shoreline are shown in figure 5 (the maximum runup and rundown occur $t \simeq 55(d/g)^{1/2}$ and $t \simeq 70(d/g)^{1/2}$). Figure 6 shows water level fluctuations at two gauge locations $X/d = 0.25$, $X/d = 9.95$. As it is clear in the figure the point $X/d = 0.25$ which is closer to initial shoreline, becomes temporarily dry during the process but the point $X/d = 9.95$ remains wet throughout the entire length of the numerical simulation. Table 3 shows the normalized root mean square deviation (NRMSD) and maximum wave amplitude errors of the numerical results compared to the analytical solutions.

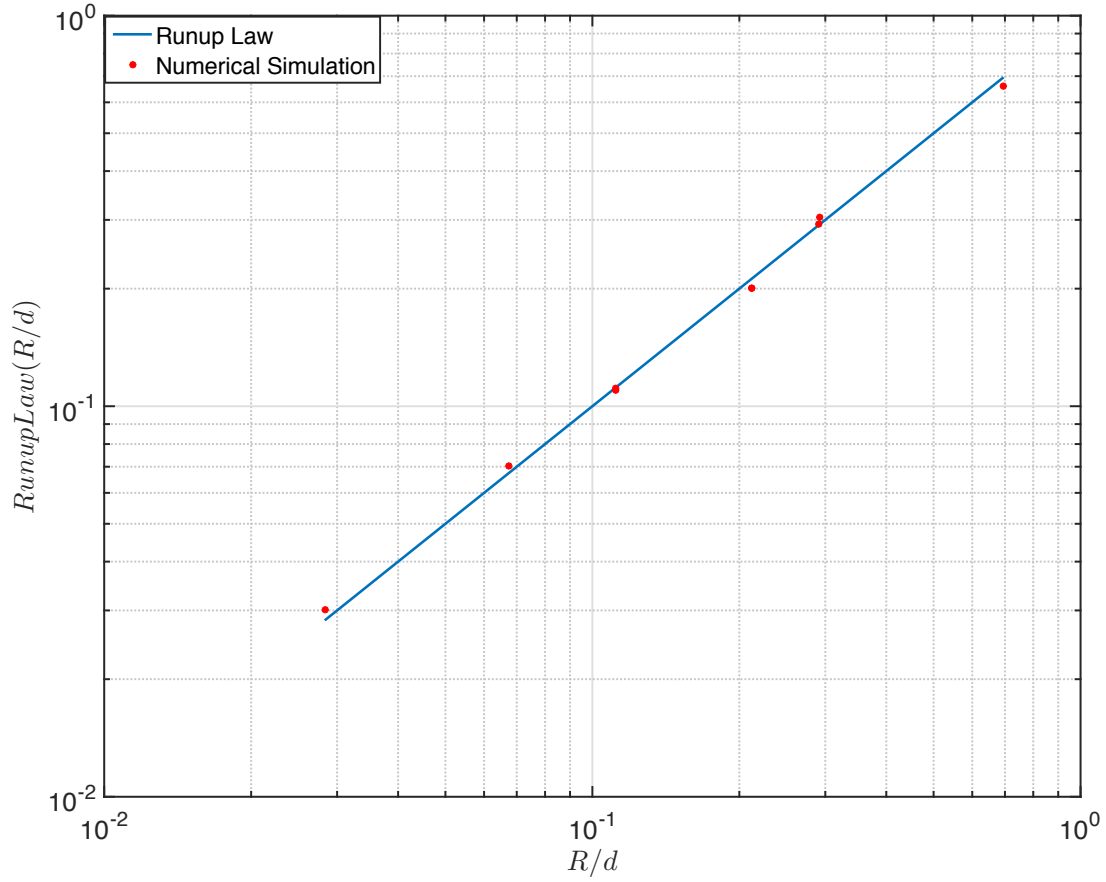


Figure 4: Numerical simulation data for maximum runup of nonbreaking waves climbing up different beach slopes. Solid line represents the runup law (25).

Water level profiles in the case of $H/d = 0.019$ at 7 moments							
t(sec)	35	40	45	50	55	60	65
NRMSD(%)	3.10	1.68	1.18	0.70	0.62	0.36	5.06
Err. max amp.(%)	0.94	0.05	1.94	4.35	1.91	2.50	0.43

Time history of wave elevation at two locations		
locations	$X/d = 0.25$	$X/d = 9.95$
NRMSD(%)	3.40	2.60
Err. max amp.(%)	1.23	1.59

Table 3: NRMSD and maximum wave amplitude errors of numerical results compared to analytical solutions.

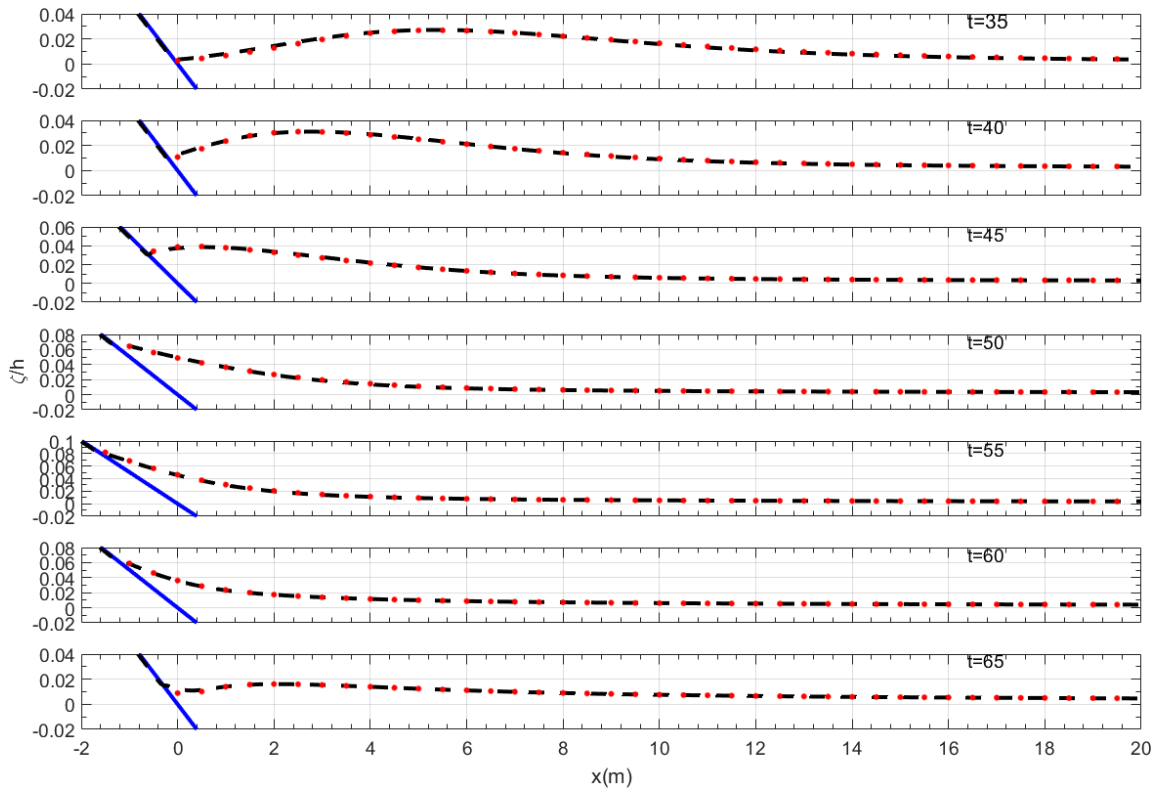


Figure 5: Water level profiles during runup of the non-breaking wave in the case of $H/d = 0.019$ on a 1:19.85 beach. Dotted red lines represent the analytical solution in according to Synolakis(1986), dashed black lines represent the numerical simulation, and solid blue lines represent the beach.

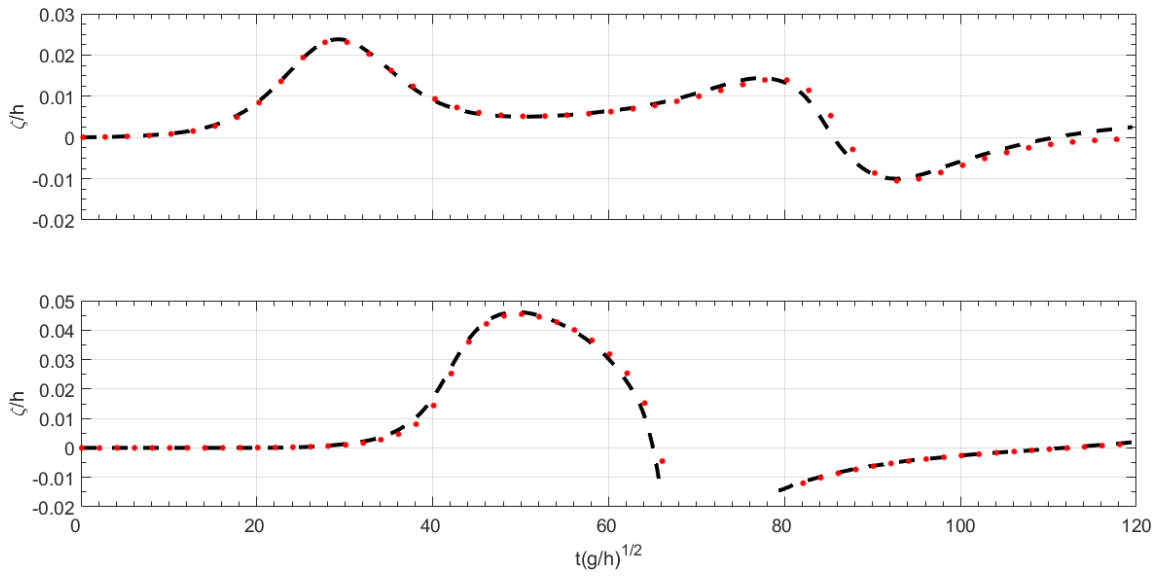


Figure 6: The water level dynamics at two locations $X/d = 0.25$ (top) and $X/d = 9.95$ (bottom). Dotted red lines represent the analytical solution in according to Synolakis(1986), and dashed black lines represent the numerical simulation.

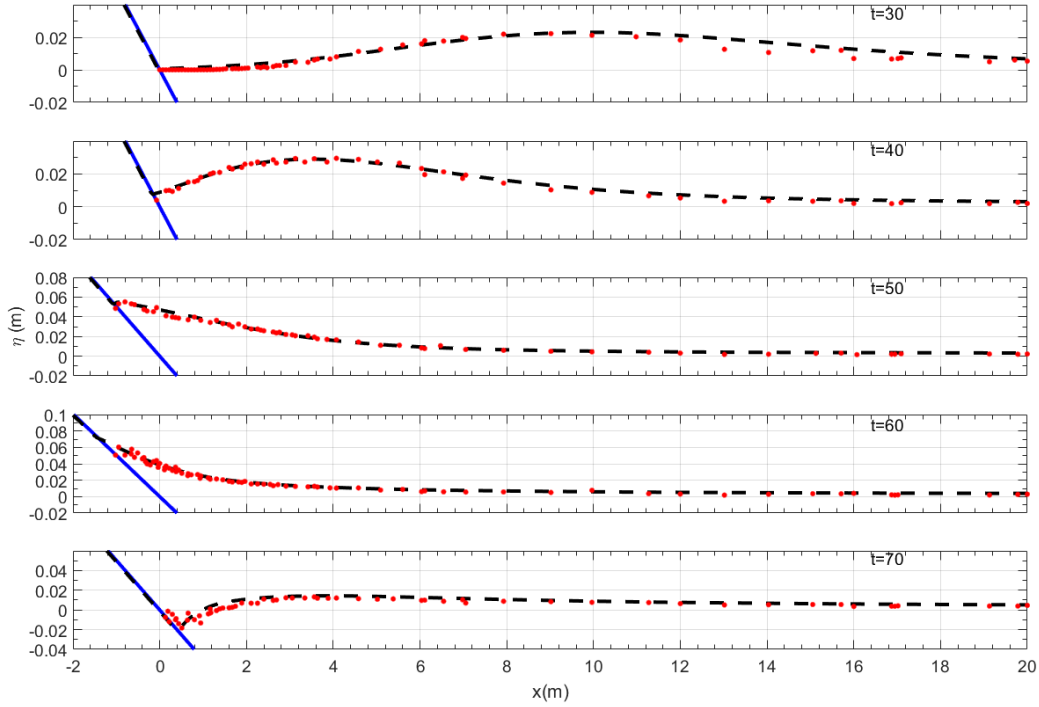


Figure 7: Time evolution of nonbreaking $H/d = 0.0185$ initial wave. Dotted red lines represent the experimental data, dashed black lines represent the numerical simulation, and solid blue lines represent the beach.

4.2 Solitary wave on a planar laboratory beach

In this laboratory test, the 31.73 m-long, 60.96 cm-deep and 39.97 cm wide California Institute of Technology, Pasadena, California wave tank was used with water at varying depths. The tank is described by Synolakis (1986, 1987). The bottom of the tank consisted of painted stainless steel plates. A ramp was installed at one end of the tank to create a sloping beach. The ramp had a slope of 1:19.85. The ramp was sealed to the tank side walls. The toe of the ramp was located 14.95 m from the rest position of the piston generator used to generate waves.

This set of laboratory data has been extensively used for many model code validations. In this model test, the data sets for non-breaking solitary waves (with $\tilde{H}/\tilde{d} = 0.0185$) and breaking solitary waves (with $\tilde{H}/\tilde{d} = 0.30$) are used. For these cases, a grid size of $\Delta x = 0.05$ m and three σ cells has been used. The option of viscous flow is turned on, and RNG $k - \epsilon$ model is applied. Figure 7 and Figure 8 displays the accuracy of the model for both nonbreaking and breaking waves. Table 4 shows NRMSD and the maximum wave amplitude errors of the numerical results compared to the experimental data.

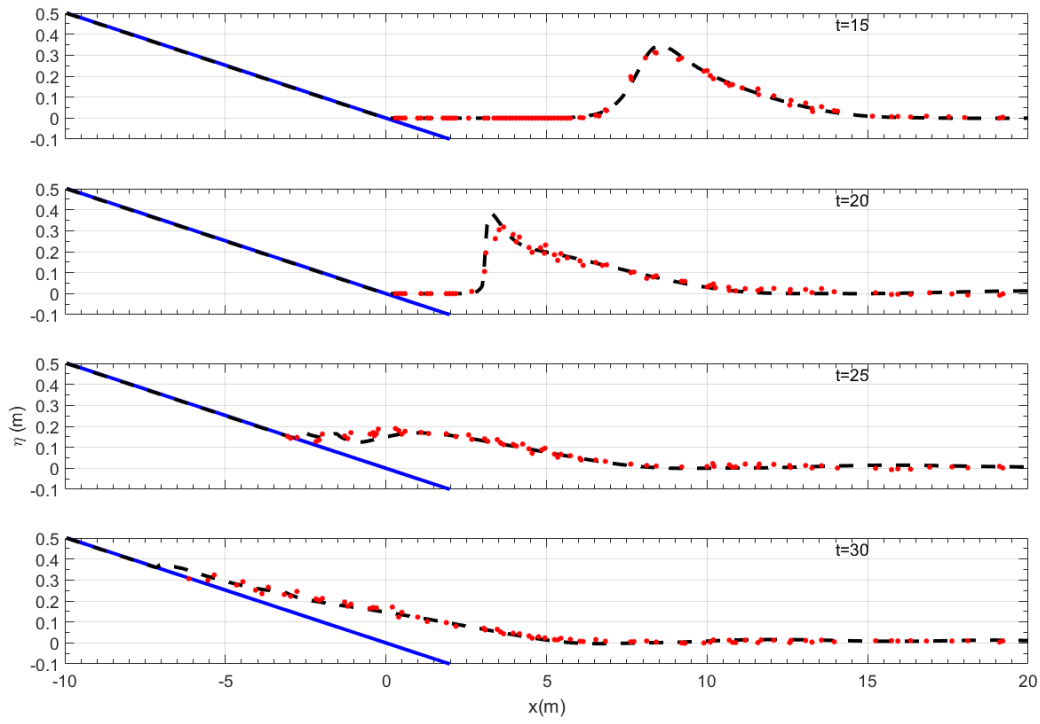


Figure 8: Time evolution of breaking $H/d = 0.3$ initial wave. Dotted red lines represent the experimental data, dashed black lines represent the numerical simulation, and solid blue lines represent the beach.

Water level profiles in the two cases at 5 moments

Cases	$H/d = 0.0185$					$H/d = 0.30$			
t(sec)	30	40	50	60	70	15	20	25	30
NRMSD(%)	10.05	5.42	3.66	4.09	14.48	2.89	6.08	7.49	3.52
Err. max amp.(%)	3.53	1.86	0.48	1.49	8.50	9.20	14.76	11.14	6.78

Table 4: NRMSD and maximum wave amplitude errors of numerical results compared to experimental data.

4.3 Solitary wave on a conical island

Laboratory experiments on the interaction between solitary waves and a conical island were conducted by Briggs et al (1995). The three cases from this test illustrate the important fact that runup and inundation heights on the sheltered back sides of an island can exceed the incident wave height on the exposed front side, due to trapping of wave fronts propagating around the island circumference. These tests have been used in a number of validation studies for a variety of models, including nonlinear shallow water equations (Liu et al 1995) and Boussinesq equations (Chen et al, 2000). The benchmark test is specified in Section 3.3 of Appendix A of Synolakis et al (2007).

Large-scale laboratory experiments were performed at Coastal Engineering Research Center, Vicksburg, Mississippi, in a 30m-wide, 25m-long, and 60cm-deep wave basin (Figure 9). In the physical model, a 62.5cm-high, 7.2m toe-diameter, and 2.2m crest-diameter circular island with a 1:4 slope was located in the basin (Figure 10). Experiments were conducted at depth of 32cm, with three different solitary waves ($H/d=0.045, 0.091, 0.181$). Water-surface time histories were measured with 27 wave gages located around the perimeter of the island (Figure 11).

For this benchmark test, time histories of the surface elevation around the circular island are given at four locations, i.e., in the front of the island at the toe (Gauge 6) and gauges closest to the shoreline with the numbers 9, 16, and 22 located at the $0^\circ, 90^\circ$, and 180° radial lines (Figure 11). A grid size of $\Delta x = 0.10m$ and 3 layers in vertical direction is considered for proper numerical simulation of this benchmark and RNG $k - \epsilon$ model is used as turbulence closure. Figures 12-14 shows the comparison between the laboratory data with numerical calculations and Table 5 shows NRMSD and the maximum wave amplitude errors between them.

Time series of free surface at 4 gauges for the 3 cases

Cases	$H/d = 0.045$				$H/d = 0.091$				$H/d = 0.181$			
	6	9	16	22	6	9	16	22	6	9	16	22
NRMSD(%)	9.67	8.85	9.43	8.75	7.99	8.20	6.75	9.38	6.58	10.33	7.17	10.94
Err. max amp.(%)	4.49	1.31	18.89	12.19	3.41	4.83	7.27	22.73	14.20	12.72	4.45	9.28

Table 5: NRMSD and maximum wave amplitude errors of numerical results compared to experimental data.

In addition, the maximum runup heights around the perimeter of the island are also compared to the laboratory data for these three cases (Figure 15) and Table 6 shows NRMSD between them.

Maximum runup heights around the island for the 3 cases			
Cases	$H/d = 0.045$	$H/d = 0.091$	$H/d = 0.181$
NRMSD(%)	16.24	17.61	14.07

Table 6: NRMSD of numerical results compared to experimental data.

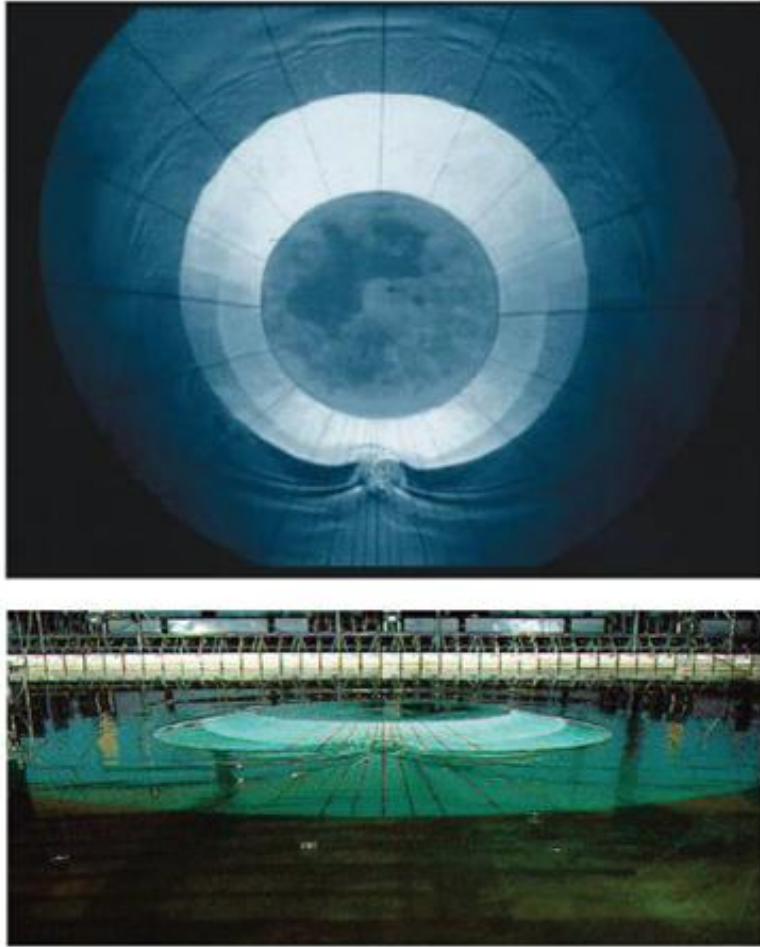


Figure 9: View of conical island(top) and basin(bottom)(from Synolakis et al (2007, Figure A16)).

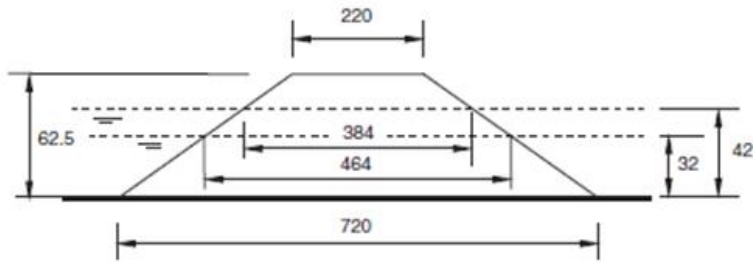


Figure 10: Definition sketch for conical island. All dimensions are in cm (from Synolakis et al (2007, Figure A17)).

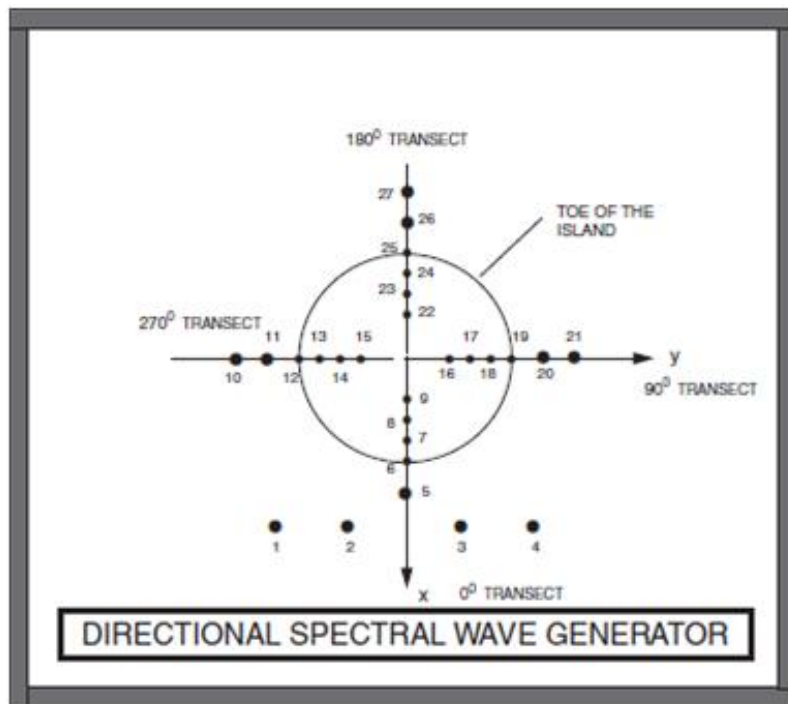


Figure 11: Schematic gauge locations around the conical island (from Synolakis et al (2007, Figure A18)).

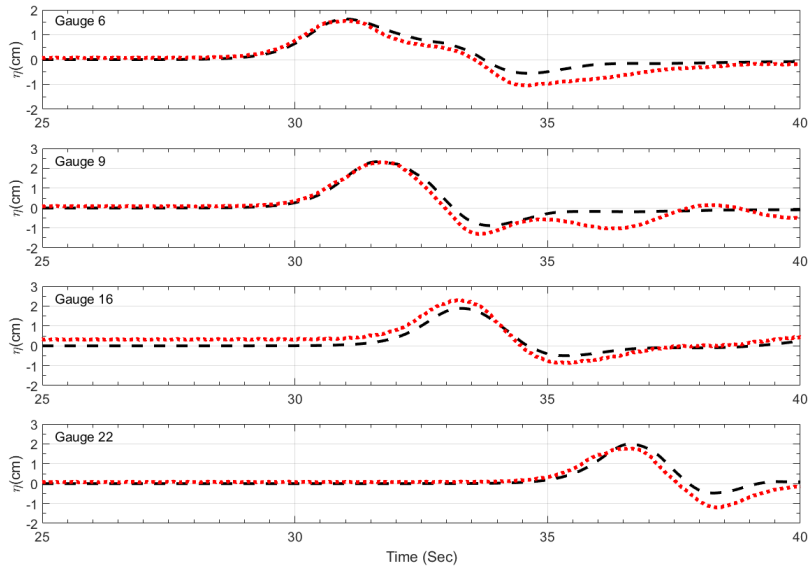


Figure 12: Comparison of computed and measured time series of free surface for $H/d = 0.045$. Dotted red lines represent the experimental data, and dashed black lines represent the numerical simulation.

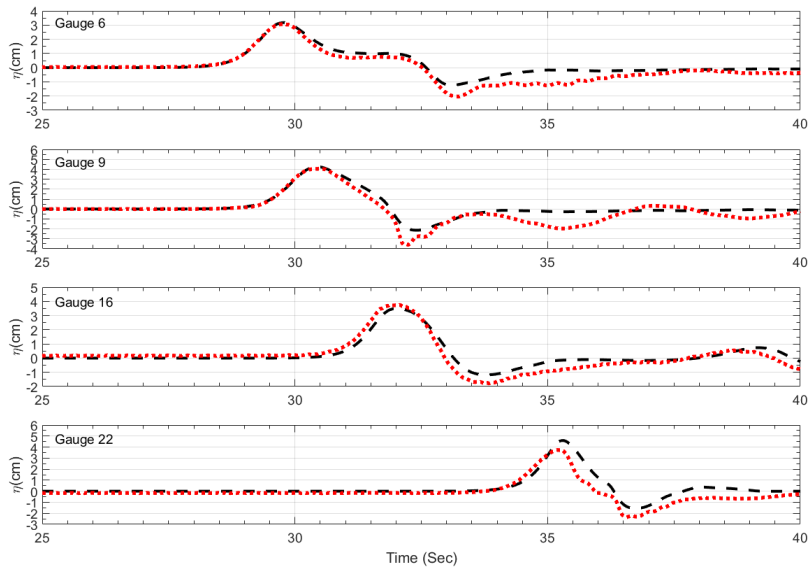


Figure 13: Comparison of computed and measured time series of free surface for $H/d = 0.091$. Dotted red lines represent the experimental data, and dashed black lines represent the numerical simulation.

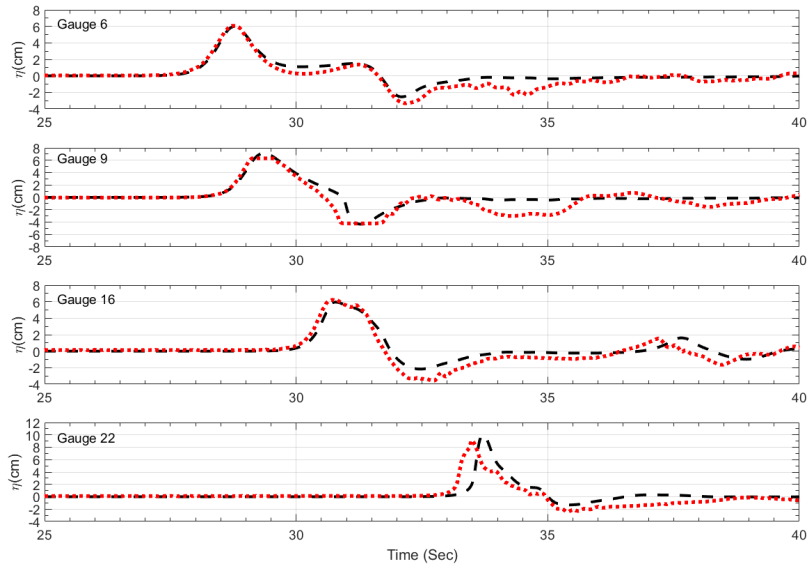


Figure 14: Comparison of computed and measured time series of free surface for $H/d = 0.181$. Dotted red lines represent the experimental data, and dashed black lines represent the numerical simulation.

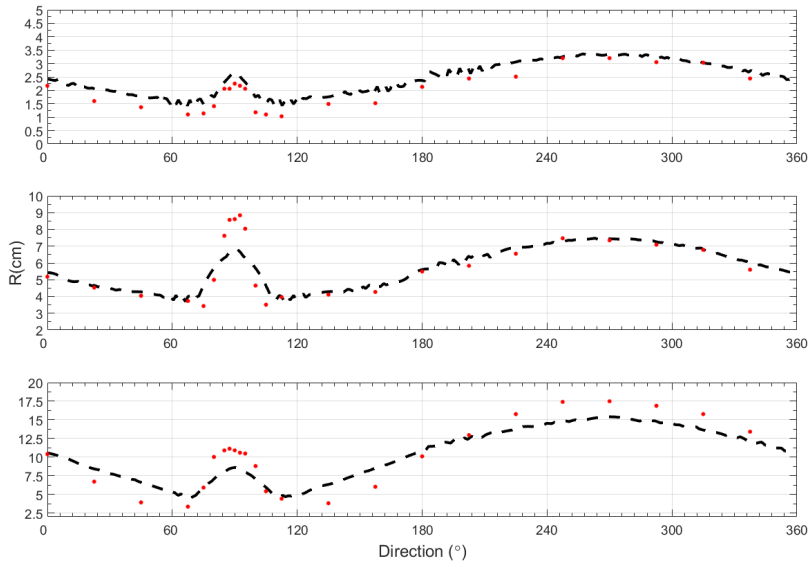


Figure 15: Comparison of computed and measured maximum runup heights for $H/d = 0.045$ (top), $H/d = 0.091$ (middle) and $H/d = 0.181$ (bottom). Dotted red lines represent the experimental data, and dashed black lines represent the numerical simulation.

4.4 Tsunami run-up onto a complex 3-D beach; Monai Valley

Motivated by the disaster in Okushiri Island, Japan, during the Hokkaido-Nansei-Oki tsunami of 1993, a laboratory experiment of Monai, where an extreme tsunami runup mark was discovered, was conducted by Central Research Institute for Electric Power Industry (CRIEPI) in Abiko, Japan. The model setup in the tank resembles to the actual bathymetry and topography around the Monai Valley in 1:400 scale and is partly shown in Figure 16. The incoming wave was generated by wave paddles away from offshore, and the wave elevations are measured at several locations by gauges.



Figure 16: Bathymetry profile of Monai Valley experiment setup (from Synolakis et al (2007, Figure A24)).

In the case, the computational domain which is $5.488m \times 3.402m$ is divided into uniform $0.014m \times 0.014m$ grid cells and the water depth is divided into 4 layers. And RNG $k - \epsilon$ turbulence model is applied. The incident wave with the water depth $d = 13.5cm$ is prescribed at $x = 0$ for the first 22.5 seconds, and the boundary conditions along $y = 0$, $y = 3.402$ and $x = 5.488$ are simply set to be wall. The incident wave generated by NHWAVE is shown in Figure 17 with the initial wave profile for the experiment.

The Figure 18 displays the comparison of five extracted frames from a video of the experiment (left) and the corresponding frame from the simulation (right), where the frame 10 occurs near 15.3 second, so on and so forth.

The time history of surface elevations are given at gauges 5, 7 and 9, i.e., located at $(x, y) = (4.521, 1.196)$, $(4.521, 1.696)$ and $(4.521, 2.196)$, and compared to the measured experimental data (Figure 19). Table 7 shows NRMSD errors between them.

Finally, the maximum runup in the small narrow galley from the simulation is 8.16cm, which is comparable to the experimental data of 7.5cm and the related field tsunami data of 30m.

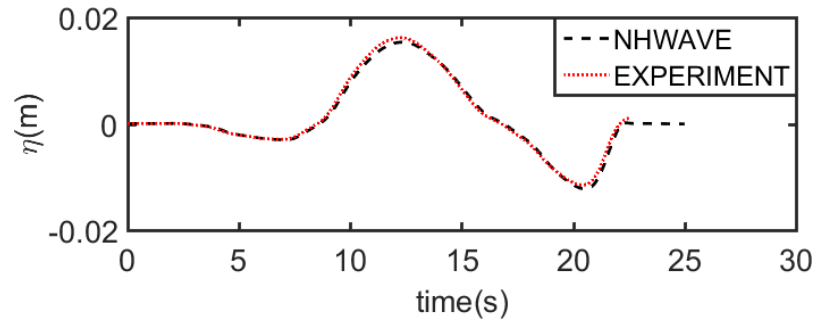


Figure 17: Initial wave profile for Monai Valley experiment and simulation.

Time history of surface elevations at 3 gauges			
Gauges	5	7	9
NRMSD(%)	14.17	11.99	10.18

Table 7: NRMSD of numerical results compared to experimental data.

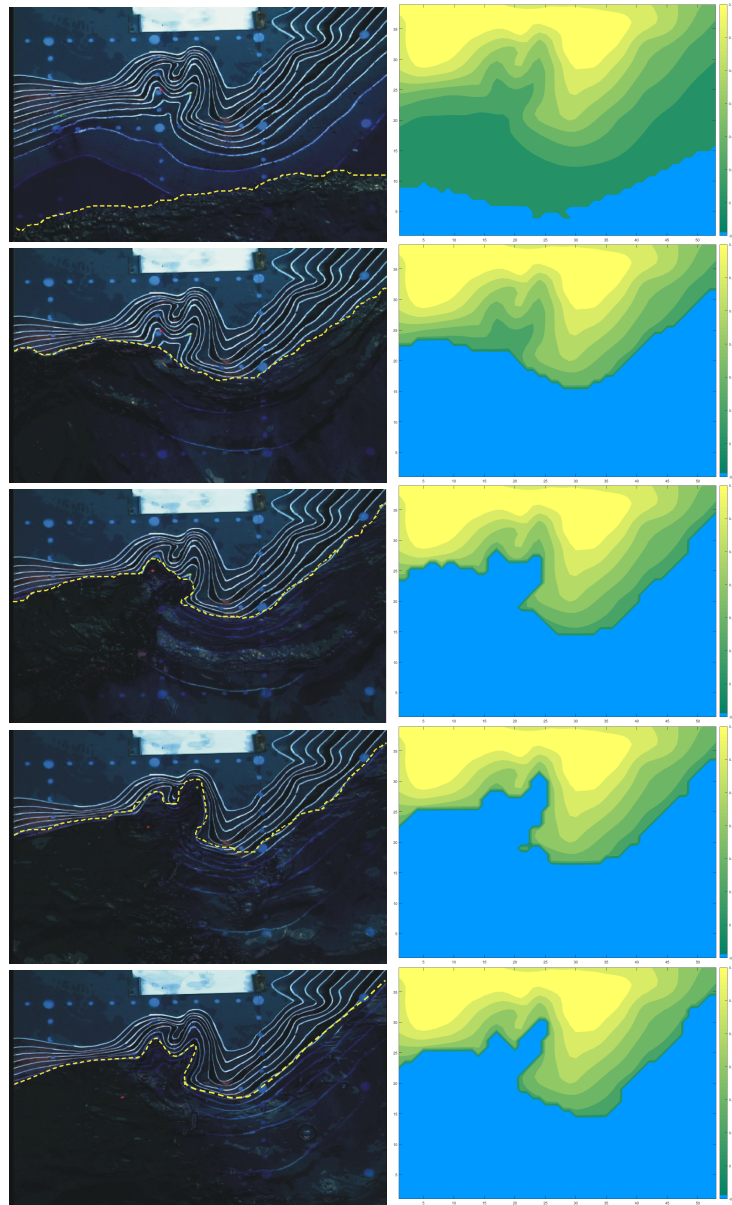


Figure 18: Comparison between extracted movie frames from the overhead movie of the laboratory experiment (left) (from [http://burn.giseis.alaska.edu/file doed/Dmitry/BM7 description.zip](http://burn.giseis.alaska.edu/file%20doed/Dmitry/BM7%20description.zip)) and numerical simulation (right).

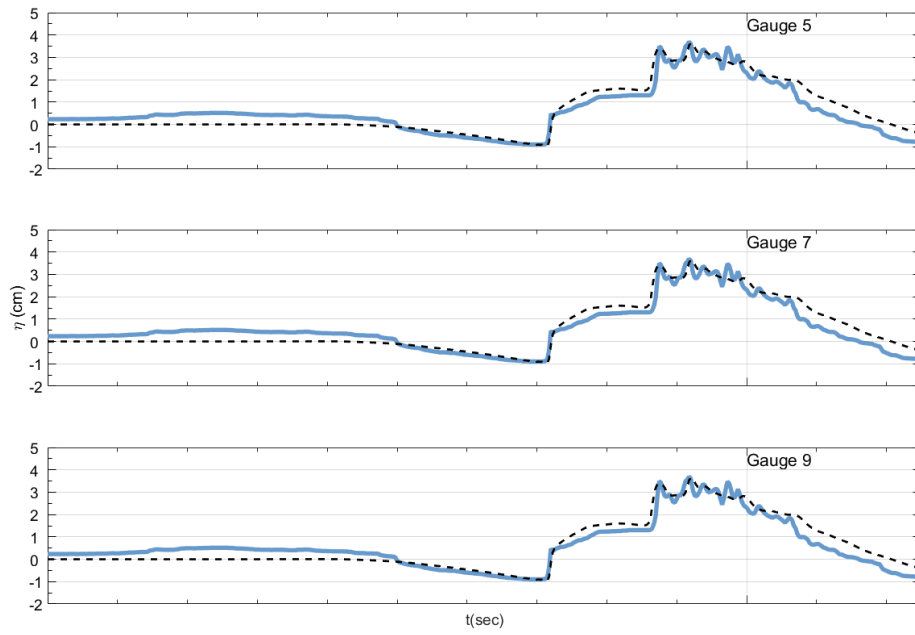


Figure 19: Time history of surface elevations at gauges 5, 7 and 9. Solid blue lines represent the experimental data, and dashed black lines represent the numerical simulation.

5 Current benchmarks

In this section, one laboratory benchmark and one field benchmark are studied as current benchmarks, and results of numerical calculations are compared to data from Lynett et al (2016). The following benchmark problems are studied in this section:

1. Flow over a submerged conical mound
2. Tsunami currents in Hilo Harbor

5.1 Flow over a submerged conical mound

The flume experiment, case SB4.02 (Figure 20), of Lloyd and Stansby (1997) has a flow field characterized by the shedding of a periodic vortex street in the wake of a submerged conical mound. NHWAVE was set up for this case in a computational domain with a width of 1.52m, length of 9.84m and depth of 5.4cm. The depth was divided into 15σ layers, and the RNG $k - \epsilon$ model of Derakhti et al. (2016a) was applied for a turbulence model. At the inflow boundary, a steady discharge velocity of 0.115m/s was specified, while, at the outflow boundary, the Orlandi radiation boundary condition is used.

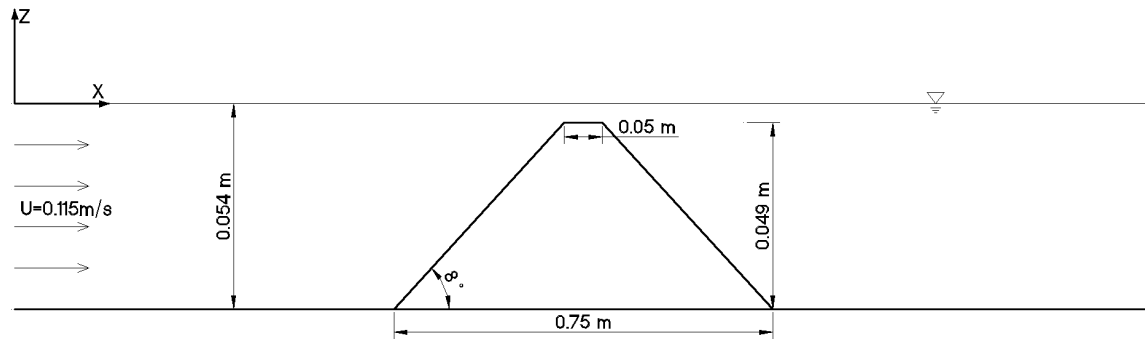


Figure 20: Definition sketch for case SB4.02 of flow over a submerged conical mound.

Our sensitivity tests indicates an decrease of grid resolution leads to growth in the flow speed and reduction in the oscillation period. Convergence of results was generally found at a resolution of 0.015m. The time step size has little effect as long as the CFL condition is satisfied. Then, several tests were carried out with different bottom roughness heights ($k_s = 0.0\text{mm}$, 0.0015mm and 0.015mm) for the grid size of $\Delta x = \Delta y = 0.015\text{m}$ and CFL number of 0.5, and the optimal bottom roughness height was found to be $k_s = 0.015\text{mm}$ based on model/data comparisons of velocity components at measurement locations (Figure 21). Figure 22 shows the comparisons of velocity components for these different bottom roughness heights. It can be seen that a decrease of the bottom roughness height results in growth of flow speed and reduction of oscillation period. When k_s is reduced to zero, the wake behind the mound becomes chaotic, with large and irregular

eddies generated. Figure 23 shows a snapshot of the vortex train behind the mound for the case of periodic motion.

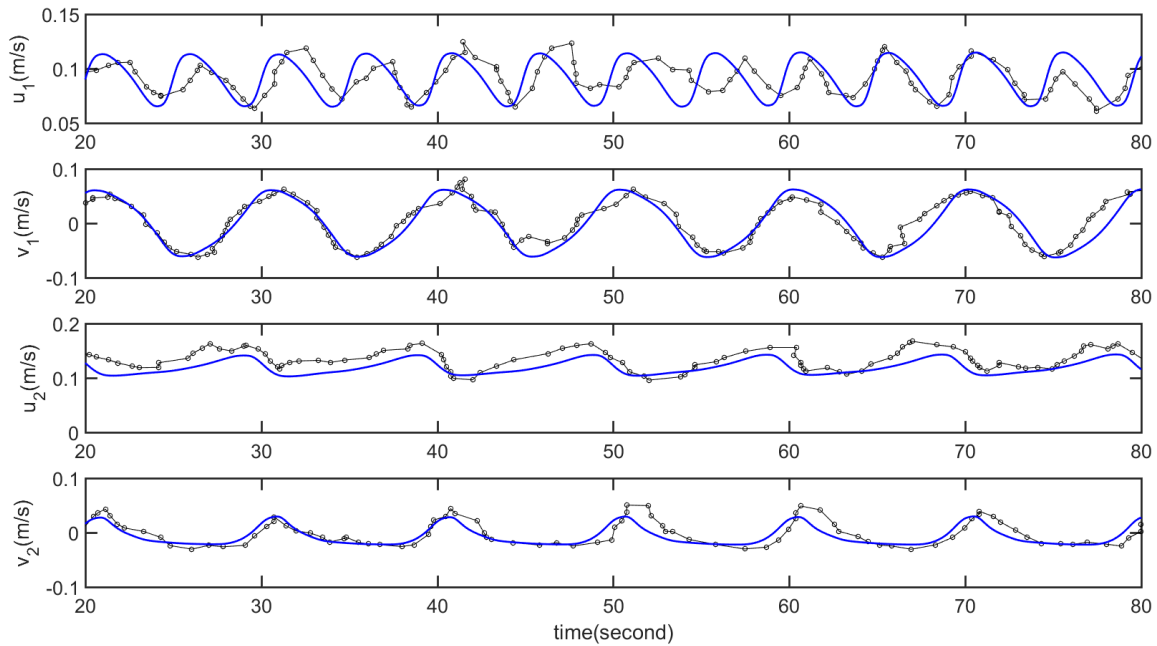


Figure 21: Comparison of velocity components between numerical results and experimental data at measurement locations. Black circles and lines represent the experimental data, and solid blue lines represent the numerical simulation.

The marked increase in streamwise surface velocity at gauge G1 seen here, relative to the values obtained in depth-integrated models such as FUNWAVE (Kirby et al., 2016) is a result of a flow pattern with strong vertical structure occurring in the wake of the mound. In the region of strongly sheared flow downstream of the mound, the horizontal shear supports an oscillatory flow with strong phase variation over depth (Figure ??). The details of this flow field are being investigated separately.

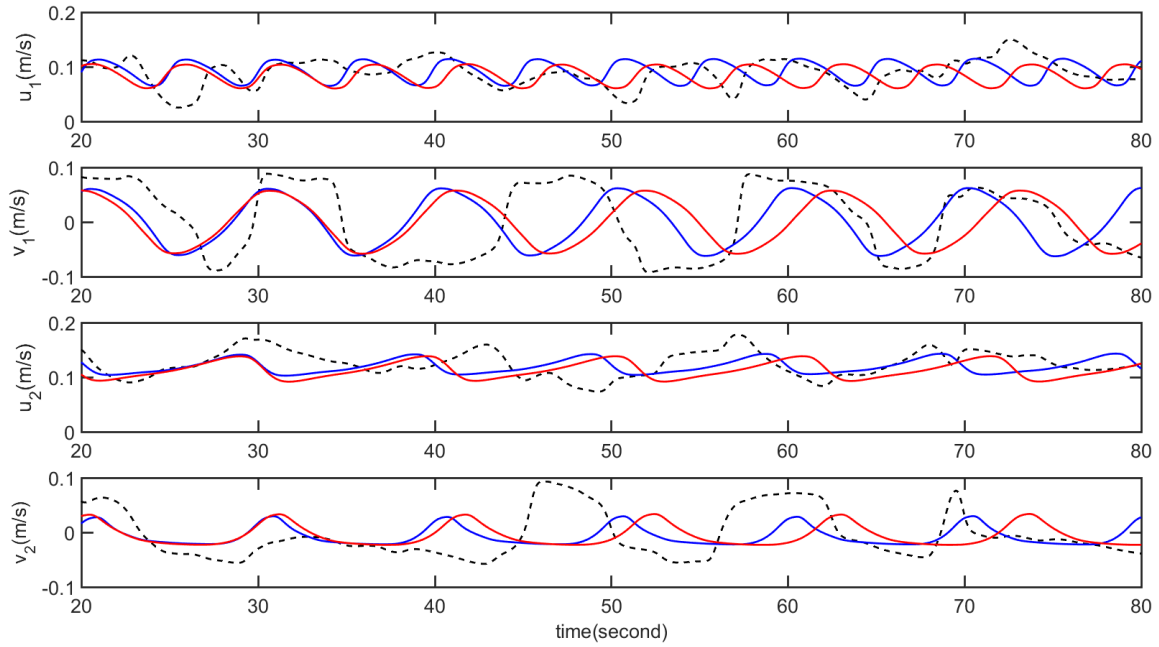


Figure 22: Comparison of velocity components for three different bottom roughness heights. Solid blue lines represent the results of $k_s = 0.0015\text{mm}$, solid red lines represent the results of $k_s = 0.015\text{mm}$, and dashed black lines represent the results of $k_s = 0.0\text{mm}$.

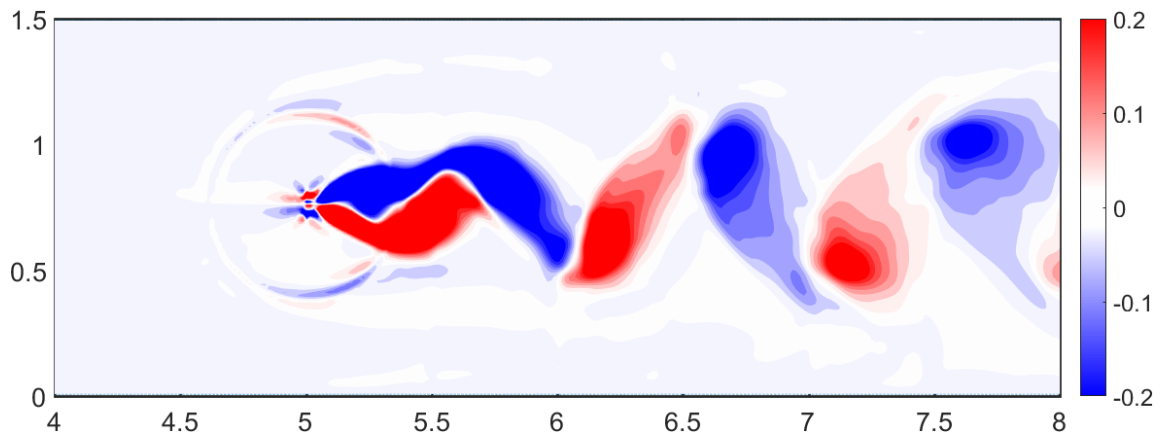


Figure 23: A snapshot of the vortex train behind the mound for $k_s = 0.0015\text{mm}$.

5.2 Tsunami currents in Hilo Harbor

This field benchmark is based on a field dataset collected during the 2011 Tohoku-oki tsunami in Hilo Harbor, Hawaii. Figure 24 shows the bathymetry data in Hilo Harbor with the simulation control point (CP), the tidal station (TG) and the two ADCP locations (ADCP1 and ADCP2) which are located on (lat, lon)= (19.7576, 204.93), (19.7308, 204.9447), (19.7452, 204.9180) and (19.7417, 204.9300) respectively. The time histories of surface elevation or velocity from observations are used as the comparison data for the simulations.

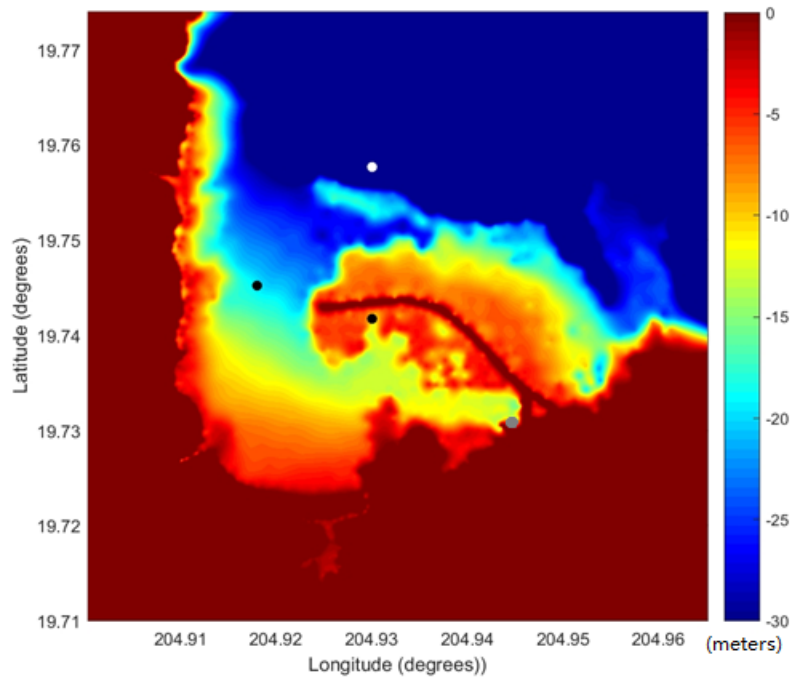


Figure 24: Bathymetry data from Hilo Harbor with the simulation control point (white dot), the tidal station (grey dot) and the two ADCP locations (black dots)(from http://coastal.usc.edu/currents_workshop/problems/prob2.html).

In order to develop boundary conditions for a simulation of Hilo Harbor using NHWAVE, we performed a simulation of the entire Tohoku event using the Boussinesq model FUNWAVE-TVD (Shi et al, 2012; Kirby et al, 2013) following procedures outlined in Grilli et al (2013) and Kirby et al (2013). A series of nested model grids with varying resolution (2 in Pacific down to 10 m in Hilo Island) were used, with intermediate results during the long-distance propagation being compared with the observational results at DART buoys. The details of this simulation can be found in current benchmark report of FUNWAVE-TVD (Kirby et al 2016).

We simulated this benchmark using NHWAVE on regular Cartesian grids with 5, 10, and 20m resolution, using grids G6, G5 and G4 described in the report (Kirby et al 2016). These grids

cover a common computational domain of 5600m wide and 6729m long, with the nesting data as the boundary conditions at north and east boundaries from Grilli's group (Kirby et al 2016), who simulated the entire event using source mechanisms described in Grilli et al (2014) and Tappin et al. (2015), and then used the FUNWAVE-TVD model in spherical coordinates (Kirby et al., 2013) to propagate the tsunami over the Pacific ocean, finally nesting down to the scale of the Hilo Harbor model. RNG $k - \epsilon$ model was applied as the turbulence model and 5 layers are set in vertical direction. The drag coefficient C_d is set to be 0.006 to include the bottom stress.

First, with the nested boundary conditions, the calculated surface elevation at CP is compared to the the observed data (Figure 25). The time history surface elevation nearly overlaps to the result from FUNWAVE-TVD and reasonably agrees with the observed data, though the nesting data introduce some errors.

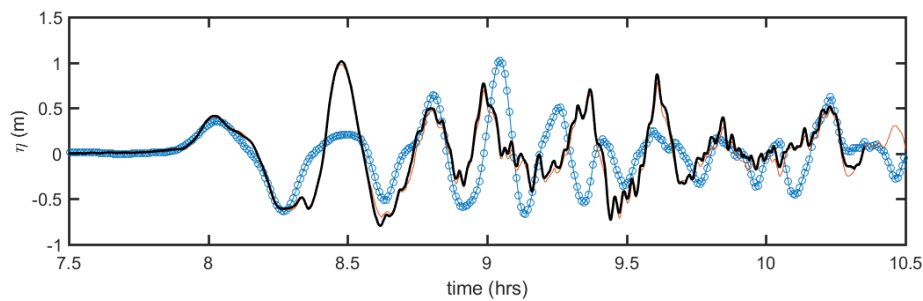


Figure 25: Time history of surface elevation at CP. Blue circles and lines represent the field data, solid red lines represent the numerical results from FUNWAVE, and solid black lines represent the numerical results from NHWAVE.

Then, the comparison between the observed data and the numerical results at TG, ADCP1 and ADCP2 are shown in Figure 26. Generally the numerical results agree the data well and are very close to the results from FUNWAVE-TVD. Figure 27 compares the numerical results from different grid G4, G5 and G6 at four points, and indicates that the resolution of grid has little effect on the results. Figure 28 shows the snapshots of vertical vorticity at ADCP1 near 8.83hr and at ADCP2 near 8.60hr with grid of G5, when maximum velocity magnitude occurs. At those two moments, an eddy with positive vorticity and one with negative are passing the two profilers respectively. And Figure 29 shows the maximum predicted fluid speed during entire duration of the 10-m resolution (G5) simulation.

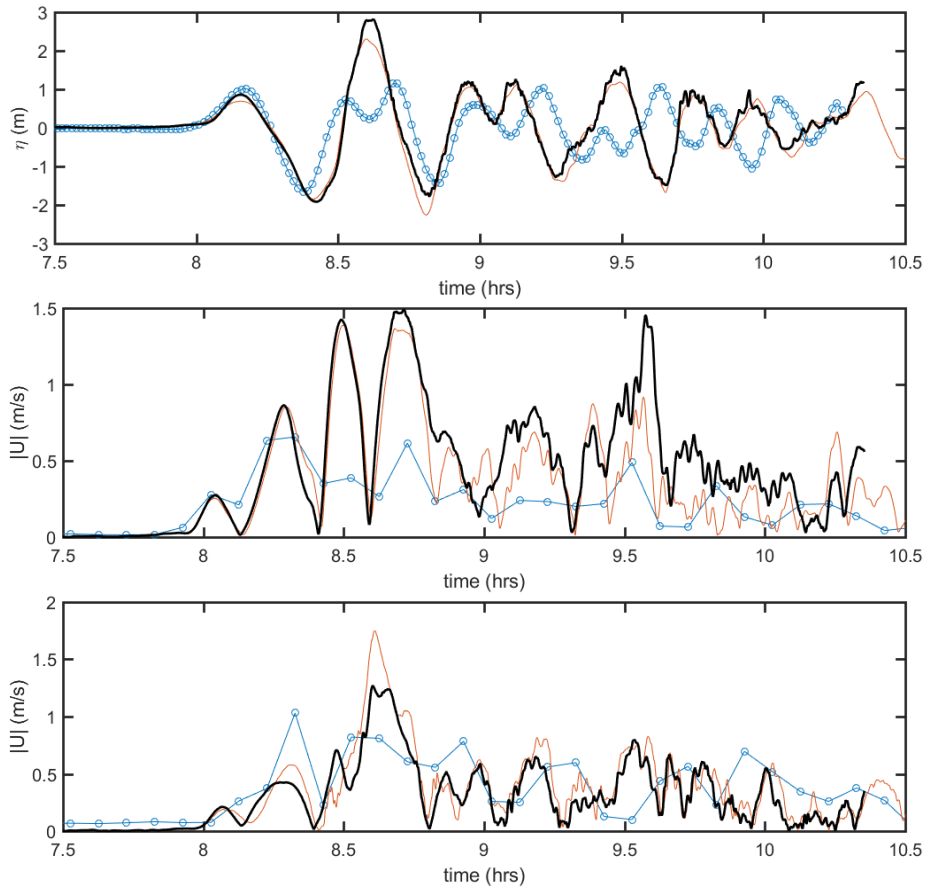


Figure 26: Time histories of surface elevation at TG (top) and of velocity magnitude at ADCP1 (middle) and ADCP2 (bottom). Blue circles and lines represent the field data, solid red lines represent the numerical results from FUNWAVE, and solid black lines represent the numerical results from NHWAVE.

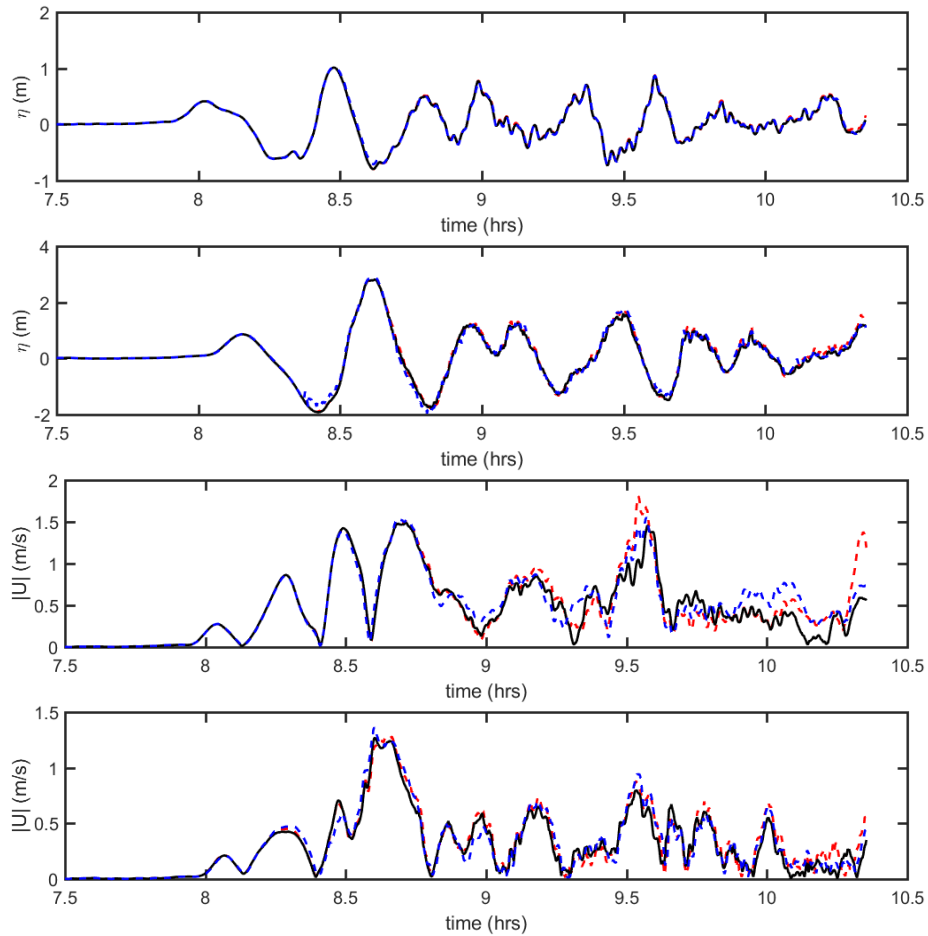


Figure 27: Comparison of results from grid G4, G5 and G6 at CP (first layer), TG (second layer), ADCP1 (third layer) and ADCP2 (last layer). Dashed blue lines represent the results with grid G4, solid black lines represent the results with grid G5, and dashed red lines represent the results with grid G6.

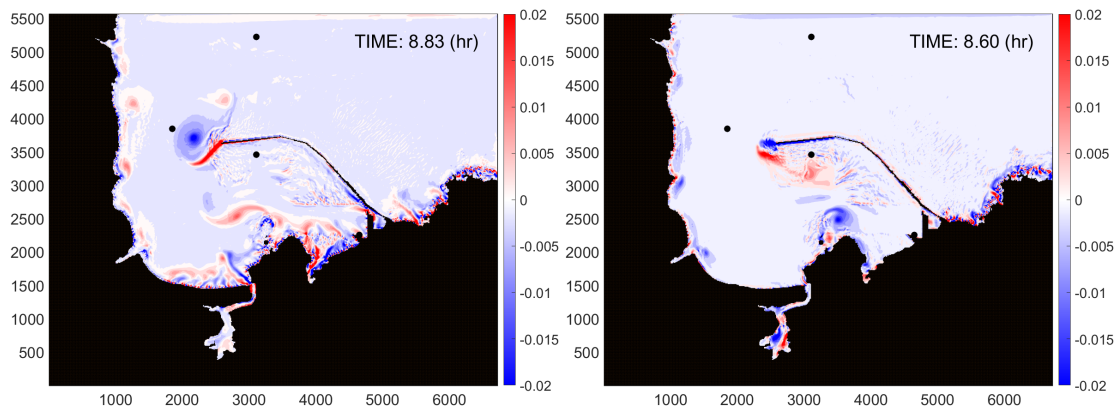


Figure 28: Snapshots of vertical vorticity at two moments showing ADCP1 (left dot) and ADCP2 (middle dot) with G5.

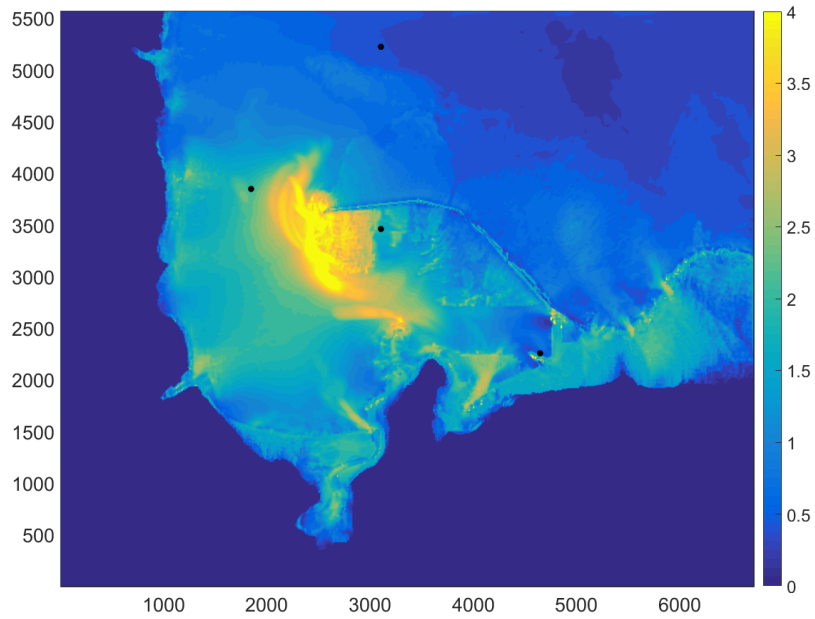


Figure 29: Maximum predicted fluid speed during entire duration of the 10-m resolution (G5) simulation.

6 Conclusions

NHWAVE has been shown to be an accurate predictor of inundation and current generation in comparison to benchmarks mandated by NTHMP. Current benchmark 1, for the Lloyd and Stansby (1997) experiment, shows the degree of depth variation that can be expected to occur in sheared shallow flows. This case is being considered in more detail using higher resolution NHWAVE simulations.

NHWAVE has been further tested against landslide tsunami benchmarks developed for the NTHMP Landslide Tsunami Model Workshop in January 2017 (<http://www.udel.edu/kirby/landslide/>). These results will be reported separately.

References

- Bradford, S. F., 2005, 'Godunov-based model for nonhydrostatic wave dynamics', *J. Waterway, Port, Coast. Ocean Engrng*, **131**(5), 226-238.
- Briggs, M. J., Synolakis, C. E., Harkins, G. S. and Green, D., 1995, "Laboratory experiments of tsunami runup on a circular island", *Pure Appl. Geophys.*, **144**, 569-593.
- Chen, Q., Kirby, J. T., Dalrymple, R. A., Kennedy, A. B. and Chawla, A., 2000, "Boussinesq modelling of wave transformation, breaking and runup. II: Two horizontal dimensions", *J. Waterway, Port, Coast. Ocean Engrng*, **126**, 48-56.
- Derakhti, M., Kirby, J. T., Shi, F., and Ma, G., 2016a, "NHWAVE: Consistent boundary conditions and turbulence modeling", *Ocean Modelling*, **106**, 121-130.
- Derakhti, M., Kirby, J. T., Shi, F. and Ma, G., 2016b, "Wave breaking in the surf zone and deep water in a non-hydrostatic RANS model. Part 1: Organized wave motions", *Ocean Modelling*, **107**, 125-138, doi:10.1016/j.ocemod.2016.09.001.
- Derakhti, M., Kirby, J. T., Shi, F. and Ma, G., 2016c, "Wave breaking in the surf zone and deep water in a non-hydrostatic RANS model. Part 2: Turbulence and mean circulation", *Ocean Modelling*, **107**, 139-150, doi:10.1016/j.ocemod.2016.09.011.
- Gottlieb, S., Shu C.-W., and Tadmor, E., 2001, "Strong stability-preserving high-order time discretization methods", *SIAM Review*, **43** (1), 89 - 112.
- Grilli, S. T., Harris, J. C., Tajalli Bakhsh, T., Masterlark, T. L., Kyriakopoulos, C., Kirby, J. T. and Shi, F., 2013, "Numerical simulation of the 2011 Tohoku tsunami based on a new transient FEM co-seismic source: Comparison to far- and near-field observation", *Pure and Applied Geophysics*, **170**, 1333-1359, doi:10.1007/s00024-012-0528-y.
- Harten A., Lax P. and van Leer B., 1983, "On upstream differencing and Godunov-type schemes for hyperbolic conservation laws", *SIAM Review*, **25**, 35.
- Kim, D. H., Cho, Y. S. and Kim, H. J., 2008, "Well balanced scheme between flux and source terms for computation of shallow-water equations over irregular bathymetry", *J. Eng. Mech.*, **134**, 277-290.
- Kirby, J. T., Shi, F., Tehranirad, B., Harris, J. C. and Grilli, S. T., 2013, "Dispersive tsunami waves in the ocean: model equations and sensitivity to dispersion and Coriolis effects", *Ocean Modelling*, **62**, 39-55.
- Kirby, J. T., Shi, F., Nicolisky, D. and Misra, S., 2016, "The 27 April 1975 Kitimat, British Columbia submarine landslide tsunami: A comparison of modeling approaches", *Landslides*, doi:10.1007/s10346-016-0682-x.

- Kirby, J. T., Shi, F., Grilli, S. T., Nemati, F. and Tehranirad, B., 2016, "NTHMP Current Benchmark Workshop: FUNWAVE TVD results", Research Report No. CACR-16-01, Center for Applied Coastal Research, University of Delaware.
- Liang, Q. and Marche, F., 2009, "Numerical resolution of well-balanced shallow water equations with complex source terms", *Adv. Water Res.*, **32**, 873 - 884.
- Lin P. and Liu P.L.-F., 1998, "A numerical study of breaking waves in the surf zone", *J. Fluid Mech.*, **359**, 239-264.
- Liu, P. L.-F., Cho, Y. S., Briggs, M. S., K anođlu, U. and Synolakis, C. E., 1995, "Runup of solitary waves on a circular island", *J. Fluid Mech.*, **320**, 259-285.
- Lloyd, P. M., and Stansby, P. K., 1997, "Shallow-water flow around model conical islands of small side slope. II: Submerged", *Journal of Hydraulic Engineering*, **123(12)**, 1068-1077.
- Lynett, P. J., et al., 2016, "Inter-model analysis of tsunami-Induced coastal currents", submitted to *Ocean Modelling*.
- Ma, G., Shi, F., and Kirby, J. T., 2012, "Shock-capturing non-hydrostatic model for fully dispersive surface wave processes", *Ocean Modelling*, **43**, 22-35.
- NTHMP, 2012, "National Tsunami Hazard Mitigation Program. Proceedings and Results of the 2011 NTHMP Model Benchmarking Workshop", NOAA-NTHMP, Boulder: U.S. Department of Commerce/NOAA/NTHMP; (NOAA Special Report), 436 pp.
- NTHMP, 2015, "Report on the 2015 NTHMP Current Modeling Workshop", NOAA-NTHMP, 212 pp.
- Patankar, S., 1980, "Numerical heat transfer and fluid flow". CRC press.
- Phillips, N. A., 1957, "A coordinate system having some special advantages for numerical forecasting", *Journal of Meteorology*, **14(2)**, 184-185.
- Russel, J.S., 1845, "Report on waves", *Rp. Meet. Brit. Assoc. Adv. Sci. 14th*, 311- 390, John Murray, London.
- Shi, F., Kirby, J. T., Harris, J. C., Geiman, J. D. and Grilli, S. T., 2011, "A high-order adaptive time-stepping TVD solver for Boussinesq modelling of breaking waves and coastal inundation", *Ocean Modelling*, **43**, 36-51.
- Stelling G. and Zijlema M., 2003, "An accurate and efficient finite-difference algorithm for non-hydrostatic free-surface flow with application to wave propagation", *Int. J. Numer. Meth. Fluids*, **43**, 1-23.

- Synolakis, C.E., 1986, "The runup of long waves", Ph.D. Thesis, California Institute of Technology, Pasadena, California, 91125, 228 pp.
- Synolakis, C.E., 1987, "The runup of solitary waves", *J. Fluid Mech.*, **185**, 523-545.
- Synolakis, C. E., Bernard, E. N., Titov, V. V., Kânoğlu, U. and González, F. I., 2007, "Standards, criteria, and procedures for NOAA evaluation of tsunami numerical models", NOAA Tech. Memo. OAR PMEL-135, Pacific Marine Env. Lab., Seattle.
- Tappin, D. R., Grilli, S. T., Harris, J. C., Geller, R. J., Masterlark, T., Kirby, J. T., Shi, F., Ma, G., Thingbaijam, K. K. S. and Mai, P. M., 2014, "Did a submarine landslide contribute to the 2011 Tohoku tsunami?", *Marine Geology*, 357, 344-361, doi:10.1016/j.margeo.2014.09.043
- Yakhot, V. Orszag, S. A., Thangam, S., Gatski, T. B., and Speziale, C. G., 1992, "Development of turbulence models for shear flows by a double expansion technique", *Physics of Fluids A: Fluid Dynamics*, **4(7)**, 1510-1520.
- Yuan H. and Wu C.-H., 2004, "An implicit three-dimensional fully non-hydrostatic model for free-surface flows", *Int. J. Numer. Meth. Fluids*, **46**, 709-733.
- Zhou, J. G., Causon, D. M., Mingham C. G., and Ingram, D. M., 2001, "The surface gradient method for the treatment of source terms in the shallow-water equations", *J. Comp. Phys.*, **168**, 1-25.